

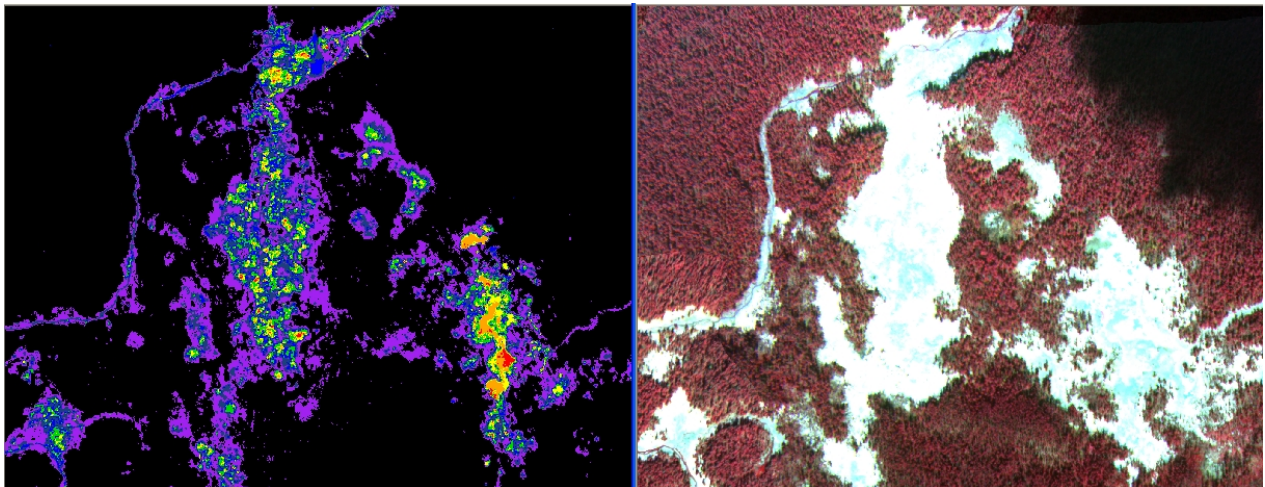
Integrated Study of Systematic Monitoring and Mapping Thermal Springs and Features in Yellowstone National Park

**Final Report for CESU Task Agreements R1580100324
From 2010 to 2011**

By

**Christopher M. U. Neale
Professor and Director of the Remote Sensing Services Laboratory
Department of Civil and Environmental Engineering, Irrigation Engineering
Division
Utah State University
Logan, UT 84322-4110**

**Submitted to
National Park Service, Yellowstone National Park
March 24, 2014**



EXECUTIVE SUMMARY

The need for accurate and continuous monitoring of geothermal activity in Yellowstone Park, led to the CESU agreement with Utah State University, to explore the use of high resolution airborne imagery for this purpose. After several years of the monitoring program a well defined methodology of image acquisition, processing and calibration has resulted in consistent quality products which is presented in the refereed journal paper included in this report. A field experiment to measure the complete energy balance of a geothermal system was installed in an explosion crater at Norris Geyser basin in 2009. This CESU covers the major period of data collection and analysis for this data set, which is being used to understand the effects of solar heating on the retrieved surface temperatures from airborne remote sensing and improve the understanding of the surface temperatures obtained from the airborne monitoring program. The ultimate goal of this effort was to be able to obtain repeatable results from year-to-year so that applications that are more sophisticated can be made with the imagery, such as heat flow calculations and accurate change detection in the geothermal areas and features. The refereed journal paper included in this report demonstrates this fact.

INTRODUCTION

The continuous monitoring of thermal features and hydrothermal areas within Yellowstone National Park is important for understanding the changing nature of these systems. Yearly monitoring provides information for protection of visitors and park personnel as well as information required for the placement of infrastructure. In addition, the data are used for scientific applications such as monitoring of hydro-geothermal explosions, heat flow calculations and change detection.

This report describes the energy balance ground based monitoring program installed in the summer of 2009 including the equipment installed in a hydrothermal explosion crater located close to the gap, Norris Geyser Basin. In addition, the airborne thermal imagery acquired during the period is also presented.

METHODS

Description of the Airborne Remote Sensing System

The present generation of the USU airborne multispectral digital system is based around three Kodak Megaplug 4.2i Digital Cameras with the imaging sensor producing digital images with approximately 2000 x 2000 pixels (Cai and Neale, 1999). The camera can be operated in 8 bits or 10 bits, but for most applications, images with 8 bits (256 grey scale levels) are sufficient. The shortwave spectral bands are obtained with interference filters centered in the green (0.545-0.560 μm), red (0.665-0.680 μm) and NIR (0.795-0.809 μm) portions of the electro-magnetic spectrum. The cameras are

mounted in a high-grade aluminum/carbon composite mount installed through a porthole in the belly of a Cessna TP206 single engine aircraft, dedicated to remote sensing. A FLIR SC640 thermal infrared camera is used to thermal images in the 8 – 12 μm range. This instrument is mounted through a different porthole aligned with the multispectral system cameras. Both the digital and thermal infrared cameras are controlled by boards and software installed in a fast PC computer with two 500 GB hard drives for storage of the imagery. Details of the multispectral system and thermal infrared camera installed in the Cessna TP206 aircraft can be seen in Figure 1.

In 2010, USU developed an integrated airborne MS system and Lidar Assisted Stereo Imager (LASSI) LIght Detection And Ranging (LiDAR) system. The LiDAR system has a full-waveform Riegl Q560 LiDAR transceiver, and a Novatel SPAN LN-200 Global positioning system (GPS)/inertial measurement unit (IMU) Navigation System. The LiDAR is capable of working up to 1200 m (4000 ft) above ground level (AGL), but for this project the aircraft flew at 700 m (2296 ft). Given the pulse rate of 100,000 shots per second, a flight speed of 185 km/h (110 mi/h) and a scan rate of 75 Hz, the result is an average shot density of 2.1 shots per square meter within a given strip. In overlap areas, this density is 2 to 3 times greater, so due to a 50% side-lap specification, an average shot return of greater than 2 shots per square meter was obtained. The LiDAR has beam divergence of less than 0.5 m rad and therefore has a footprint size of about 0.5 m at 1000 m (3300 ft) AGL. Digitized at a rate of 1 GHz, the waveform for each shot yielded a volume spacing of 0.3 m for each single shot within the vegetation. Additional processing of this waveform produced multiple points per laser shot. Four ImperX Bobcat cameras with 4904 x 3280 pixel density sensors, with interference filters forming spectral bands in the Blue (0.465-0.475 μm), Green (0.545-0.555 μm), Red (0.645-0.655 μm) and Near Infrared (NIR) (0.780-0.820 μm) acquired the MS images for the new system. (Figure 1d and 1e). Using the Terrascan and Terraphoto/Microstation software, data from the IMU system, Lidar point cloud-based Triangular Irregular Networks (TINS), and the time stamped images, rectified orthoimages are produced through direct georeferencing.

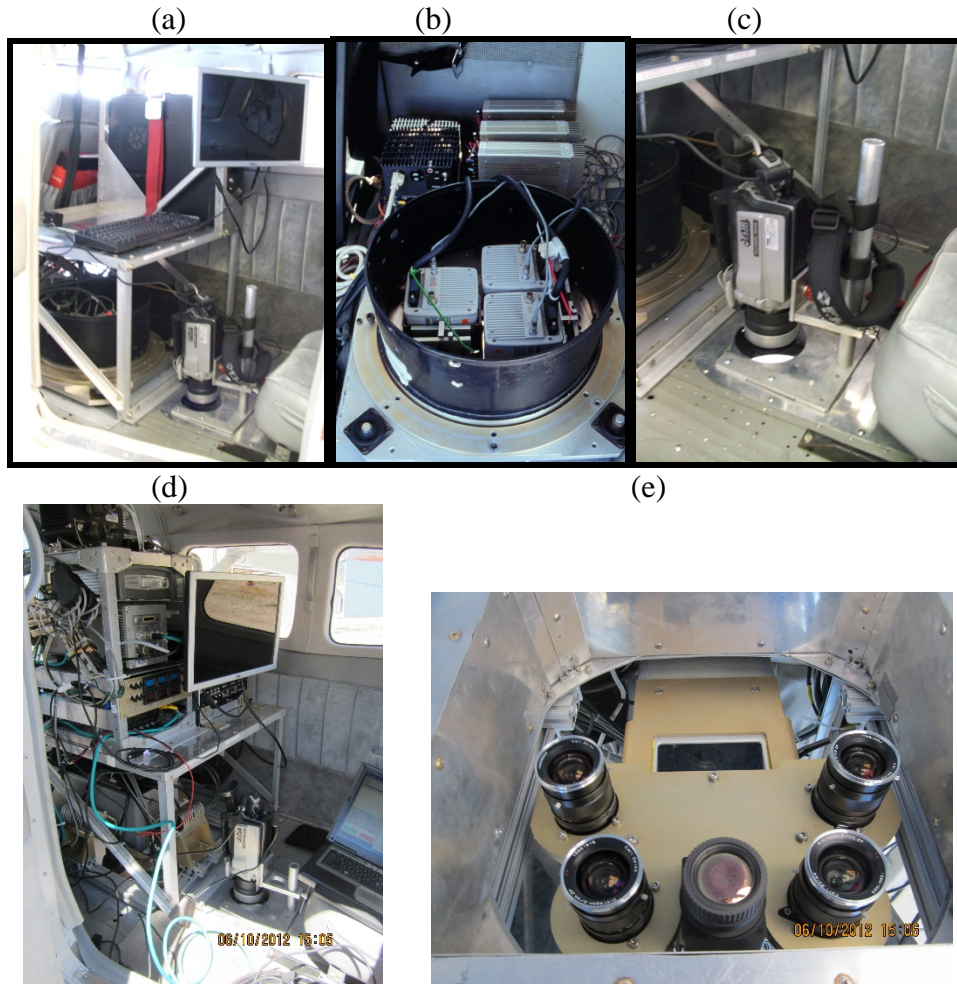


Figure 1. (a) The USU airborne multispectral (MSS) remote sensing system installed in the Cessna TP206; (b) the Kodak Megaplex 4.2i camera; (c) the FLIR SC640 thermal IR camera; (d) the LASSI integrated LiDAR/multispectral system and (e) view of the installed integrated system from below.

Image Acquisition

High-resolution shortwave (3 bands) and thermal infrared imagery were acquired with the USU airborne digital system over different areas of Yellowstone Park, according to the monitoring plan devised by the YNP technical personnel and USU. The pixel resolution in the shortwave bands (green, red and near-infrared) was 1-meter while in the thermal IR it was also 1-meter for the night-time flights. For a 1-meter pixel resolution using the 20 mm Nikon lens of the shortwave digital cameras, the flight altitude was 7000 feet above ground level (agl). Considering the ground elevations at Yellowstone over the thermal feature sites varied between 6000 and 7500 feet, the flight altitude usually varied between 13000 and 14500 feet. This required the use of oxygen masks by the pilot and co-pilot during the image acquisition. For safety reasons, the nighttime flights with the FLIR SC640 camera were conducted with a 40 mm lens so that the aircraft could operate well above the terrain.

Flight lines were planned to ensure 30% overlap between images in parallel flight lines and 80% overlap along the flight lines to guarantee complete coverage over the study areas and a flight altitude to capture the appropriate resolution at an average ground altitude along the flight line.

The nighttime image acquisition over-flights in 2010 and 2011 were conducted during the month of September, under clear sky conditions, between 11:00 pm and 3:00 am. Cold air and surface temperatures are usually rapidly reached at those altitudes and time of the year after sundown, due to irradiative cooling of the surface. This increases the contrast between the hydrothermal areas and the surrounding cooler areas.

Additional flights were conducted during the daytime between 1:45 and 3:00 pm local time under clear skies, usually the hottest time of the day, in order to acquire multispectral shortwave imagery and additional thermal imagery over new areas previously not flown. The shortwave band imagery was acquired at 1-meter spatial resolution and used to correct the temperatures obtained from the nighttime and daytime thermal imagery for surface emissivity. This process is described in the journal paper that describes the methodology annexed to the report.

In 2010, the Norris Geyser basin was flown with the USU LASSI LiDAR system along which at that point in time had been integrated with the USU airborne multispectral system. The resulting mosaic is shown later in the report.

Image Processing

The individual spectral band images from the shortwave band digital cameras of the USU system are 2012 x 2014 pixels in size, thus at 1-meter pixel resolution, each image covered an area of approximately 2 x 2 Km. The single band images were first corrected for lens vignetting effects (Neale and Crowther, 1994) and for lens radial distortions (Sundaraman and Neale, 1999) and registered into 3-band images ready for geo-rectification. This was accomplished using common control points obtained

from a digital color-IR orthophotoquad produced by the Wyoming Geographic Information Advisory Committee. A 3rd order polynomial transformation was used. The root mean square (rms) error for the individual image rectification was kept to less than one meter. The rectified images were then stitched along the flight lines forming image strips. These strips were calibrated to a reflectance standard using the system calibration obtained through a similar procedure as that described by Neale and Crowther (1994). The incoming irradiance from the sun and sky was measured every minute using an Exotech radiometer with similar spectral bands placed overlooking (from nadir) a standard reflectance panel with known bi-directional properties setup in a central location in the Park (Figure 2). Once the image strips were calibrated, they were stitched together forming a mosaic covering the entire study area.

The calibrated and rectified 3-band mosaic was then used as the base map for rectification of the thermal imagery as it was acquired on the same date and better represented the surface conditions at the time. In addition, it was important that thermal images match the 3-band mosaic as the latter would be used in the correction of the thermal image for surface emissivity.

Thermal images from the FLIR SC640 were extracted from the digital sequence files providing individual frames at 60% overlap. Each thermal image was rectified using common control points with the 3-band mosaic and then stitched together along the flight lines to form image strips. These were then calibrated using the camera calibration files to obtain at-aircraft temperatures. Several calibrated strips are then stitched together to form a mosaic covering the study area.

In the fall of 2011, while analyzing multiyear imagery to conduct change detection and heat flow calculations, it was observed that some of the digital thermal imagery had been extracted from the FLIR digital sequence files using different settings in different years. It was decided that the imagery should be extracted again with a common set of parameters and settings and imagery acquired from 2007 to 2011 would be re-processed using these common settings and re-calibrated. In addition, the radiosonde data from the Great Falls, Mt station was used instead of the Riverton, Wy as it was deemed more representative at the altitudes of Yellowstone Park. The recalibration task has now been completed and products for the 2010 and 2011 period re-submitted to the NPS.



Figure 2. Standard reflectance panel and Exotech 4-band radiometer measuring incoming irradiance from the sun setup in the Upper Geyser basin area during one of the daytime flights in Yellowstone Park.

The at-aircraft temperature image was corrected for atmospheric effects at the time of the over flight using the MODTRAN radiative transfer model (Berk et al, 1989). For such, radiosonde data from a nearby weather station (Great Falls, MT) was used to obtain the profile of air temperature, dew point temperature and pressure between the surface and the aircraft altitude, required by the model. The profile was adjusted to compensate for the differences in ground surface altitudes. The correction for surface emissivity was based on the technique by Brunsell and Gillies (2002) described in the Journal Paper in the appendix section of this report.

Energy Balance Study

Two complete energy balance flux towers were installed in the summer of 2009 in a hydrothermal explosion crater in the gap area of Norris Geyser Basin to acquire data required for studying heat flow in thermal areas. The goal was to study the relationship between heat flux and surface temperatures in dry and wet areas under solar heating. The generation of steam over hot pools was perceived as masking the ability to retrieve true surface temperatures from the airborne remote sensing requiring more study. This present research effort also covered the gathering and analysis of this data.

The installation of the two towers was carried out in June 2009. Figure 3a shows tower #1 installed on the upwind side of the crater lagoon in a hot sintered area. The

tower contained a 4-way net radiometer, a rain gauge, temperature and relative humidity sensor, soil heat flux plates and corresponding soil temperature thermocouples on 3 different areas: one very hot and two medium temperatures. In addition, thermal infrared radiometers (TIR) were pointed at the surface where the heat flux plates and temperature sensors (Figure 3b) were located as well as to the area in the lagoon where the water temperature sensor was located at the tip of a log (Figure 3c and 3d). This tower was controlled by a CR3000 datalogger from Campbell Scientific powered by a 12 volt battery maintained with a solar panel. Tower #2 shown in Figure 4a was installed downwind on the other side of the lagoon from Tower #1. Its approximate location can be seen in Figure 5b where the cursor is positioned on the image. The instrumentation installed consisted of a net radiometer (NR-Lite), temperature and relative humidity sensor, soil heat flux plates and soil temperatures sensors at two locations with corresponding TIR's pointing to the surface (Figure 4b). A water temperature sensor and corresponding TIR sensor can be seen in Figure 4d and 4c. Figure 5a shows an areal TIR image of the crater and lagoon taken with the FLIR SC640 camera. Tower #1 was located on the hot sintered mound south of the lagoon while tower #2 was placed north of the lagoon, its location approximately marked in Figure 5b.

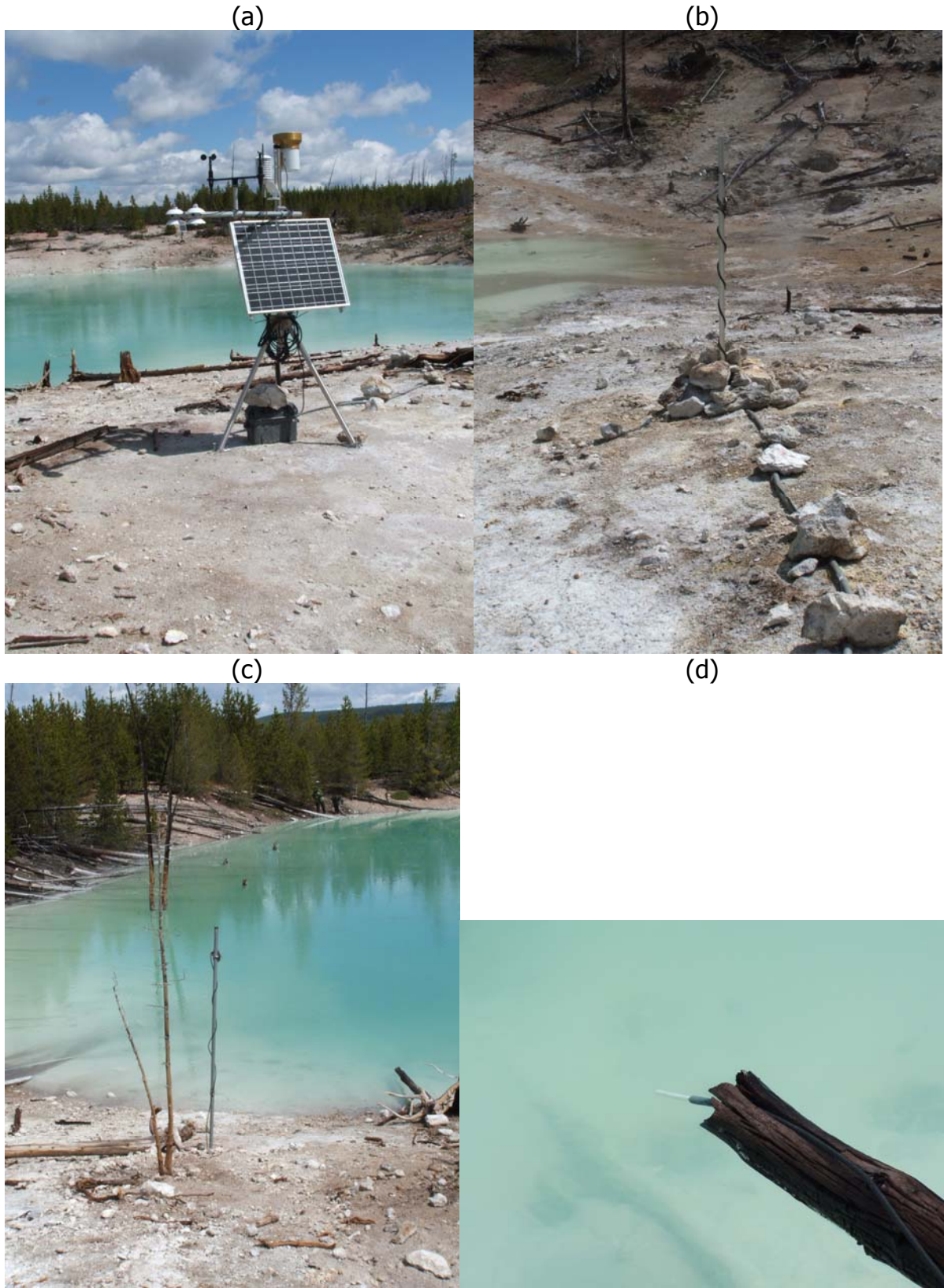


Figure 3. Energy balance tower #1 installed on the upwind side of the crater lagoon, The Gap, Norris Geyser basin.

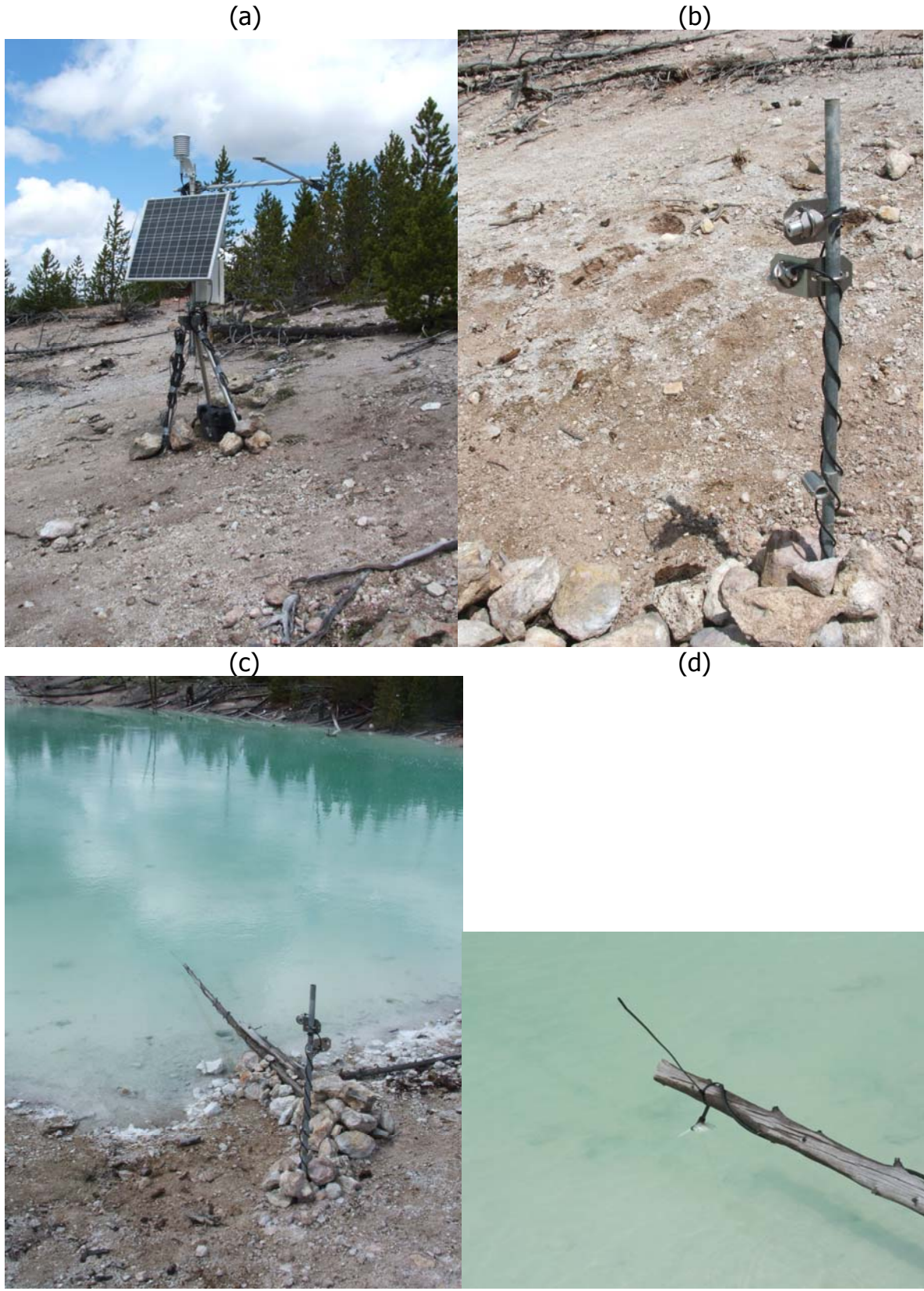


Figure 4. Energy balance tower #2, located downwind of the lagoon.

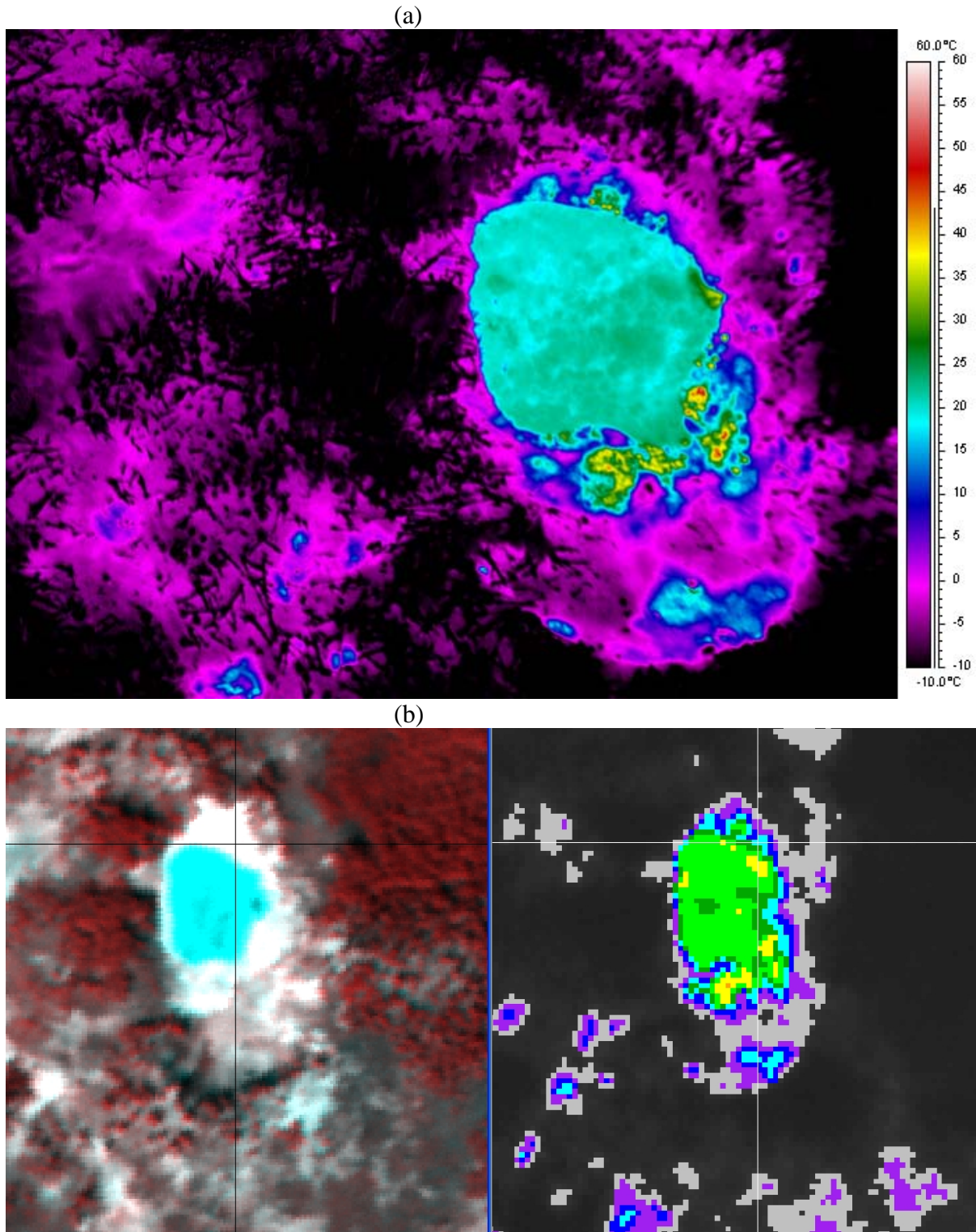


Figure 5. Oblique, daytime thermal infrared image with a NPS contract helicopter (a) visible image (b) and nighttime thermal infrared image (c) of the crater and lagoon.

IMAGE ACQUISITION DATES

Table 1 below summarizes the image acquisition flights for 2010. The new areas flown in 2010 were Mammoth Hot springs and the Gardiner River along with Sulphur Hills. The repeat areas part of the continuous monitoring were Upper Geyser Basin (UGB) and the Old Faithful area, Hot Spring Basin (HSB) and Norris Geyser Basin.

Table 1 Hydrothermal areas monitored during the 2010 campaign

Location flown	Processing Status	Observations: 2010 Image Acquisition Campaign
Mammoth	Completed & Delivered	Mutlispectral Orthoimages
Gardiner	Completed & Delivered	Mutlispectral Orthoimages
LGB	Completed & Delivered	Mutlispectral Orthoimages
Norris	Completed & Delivered	Mutlispectral Orthoimages
Sulphur Hills	Completed & Delivered	Mutlispectral Orthoimages
Old faithful	Completed & Delivered	Mutlispectral Orthoimages
Hotsprings	Completed & Delivered	FLIR camera
Sulphur Hill	Completed & Delivered	FLIR camera
Norris	Completed & Delivered	FLIR camera
Oldfaithful	Completed & Delivered	FLIR camera
Mammoth	Completed & Delivered	FLIR camera
Gardiner	Completed & Delivered	FLIR camera
LGB	Completed & Delivered	FLIR camera

RESULTS AND DISCUSSION

Samples of the delivered products for the 2010 campaign

Samples of the delivered imagery from the 2010 and 2011 campaigns will be presented in this section, processed as described in the Methods section and the Paper in the appendix section of the report. Figure 6 shows the 3band multispectral mosaic of Norris Geyser Basin produced with the integrated multispectral and LASSI LiDAR system, flown in 2010. It was produced through direct georeferencing and has improved spatial accuracy. Figure 7 shows a detail of the image at full resolution. The corresponding thermal IR image is shown in Figure 8. Figure 9, 10 and 11 show the thermal IR products for Upper Geyser Basin, Hot Springs Basin and Mammoth Hot Spring, respectively.

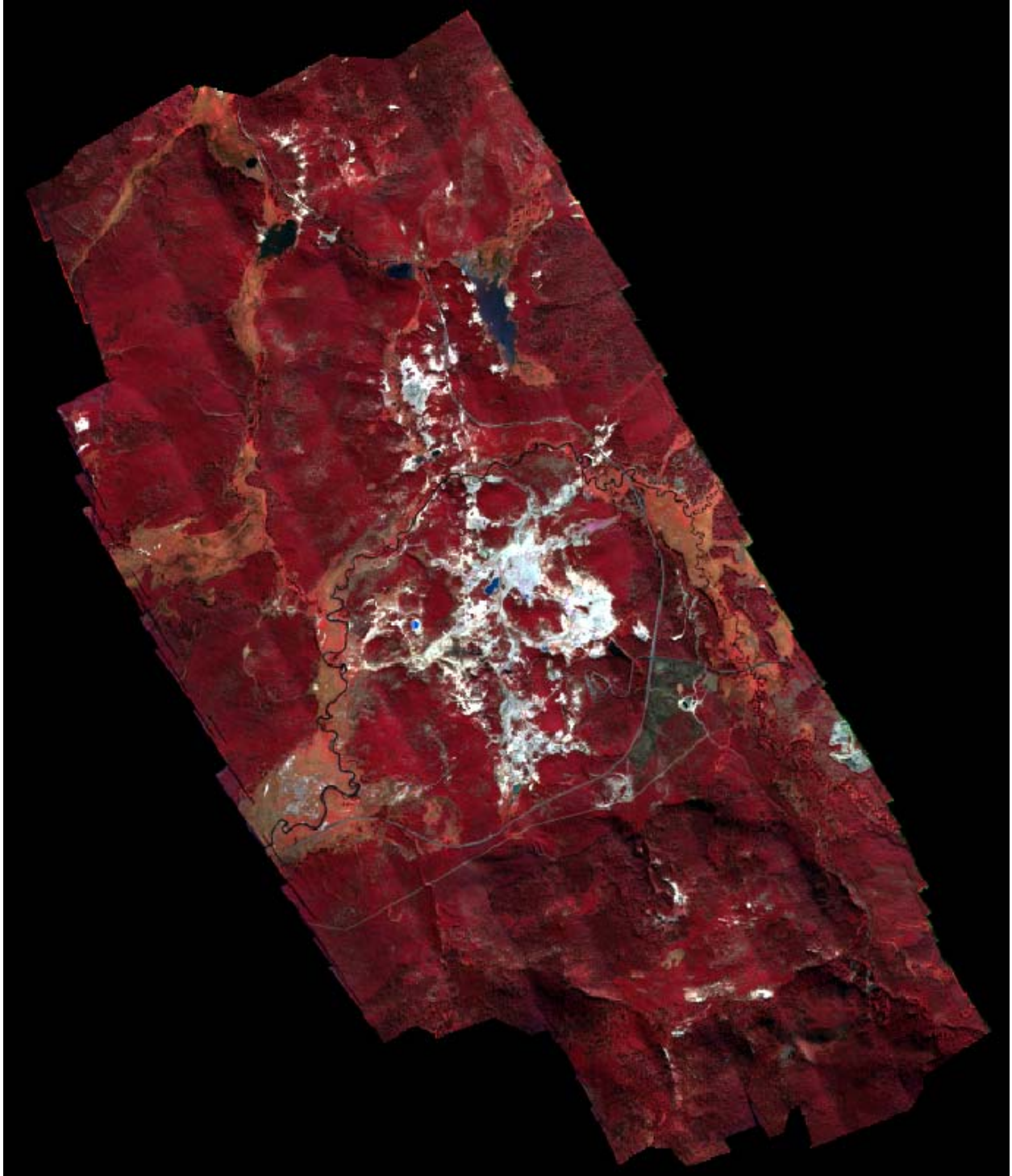


Figure 6 Multispectral mosaic of the Norris Geyser Basin using imagery acquired during the 2010 season.

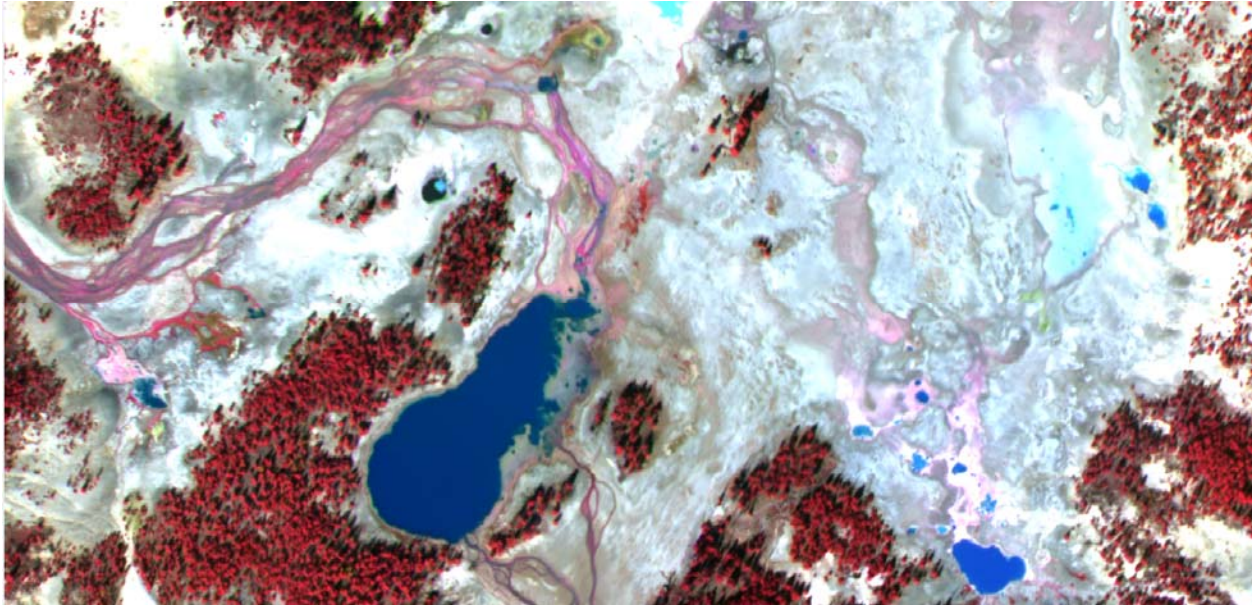


Figure 7 High-resolution detail of orthoimage produced in 2010 using LiDAR data for orthorectification with the direct georeferencing procedure.

Norris_2010

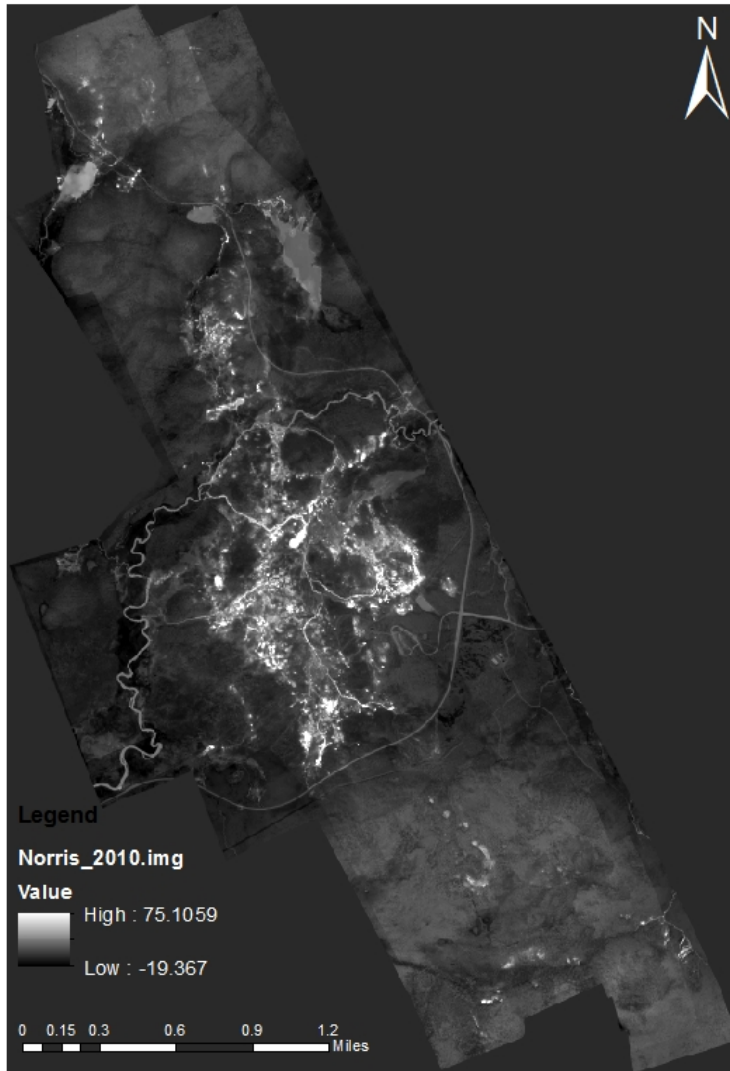


Figure 8 Calibrated and corrected radiometric surface temperature image mosaics for Norris Geyser Basin acquired in September 2010.

Upper Geyser Basin_2010



Figure 9 Calibrated and corrected radiometric surface temperature image mosaic for Upper Geyser Basin acquired in September 2010.

Hot Springs Basin_2010

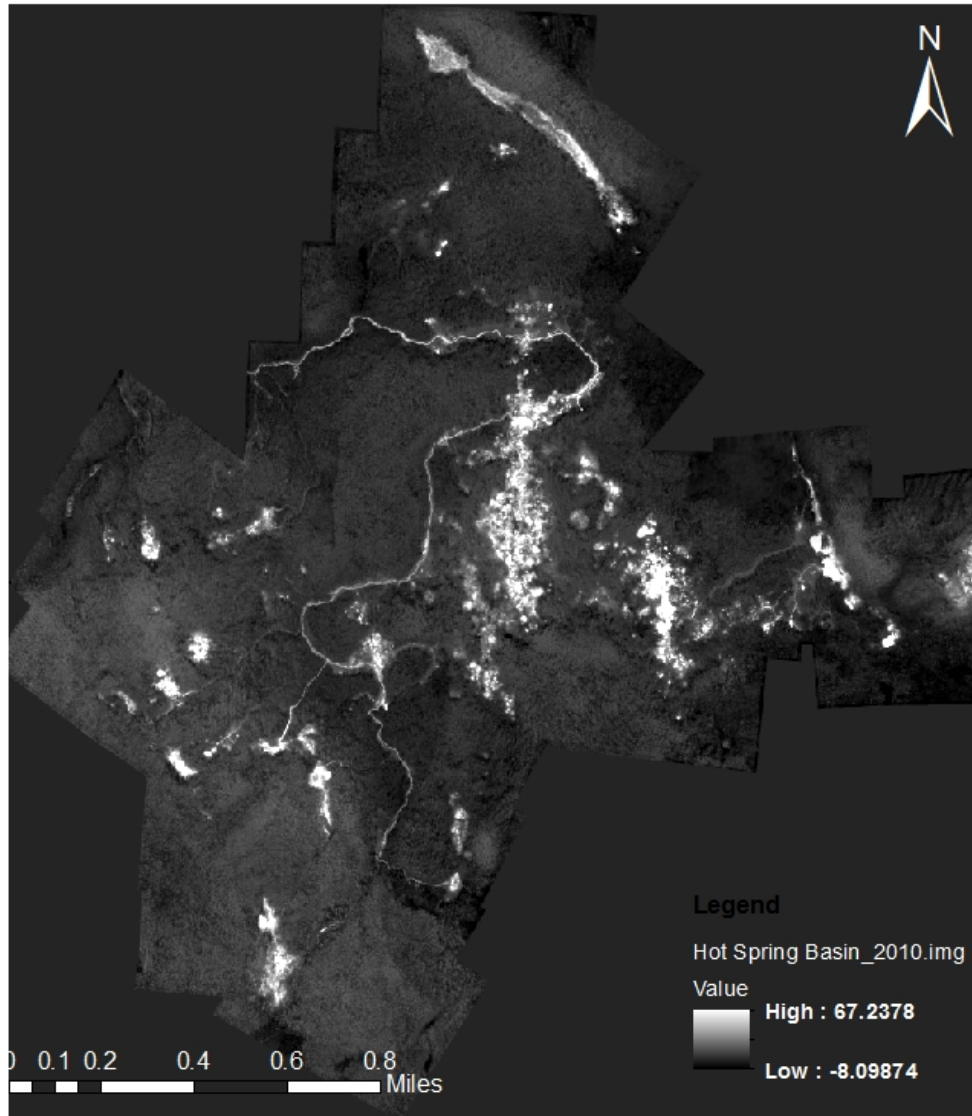


Figure 10. Calibrated and corrected radiometric surface temperature image mosaic for Hot Springs Basin acquired in September 2010.

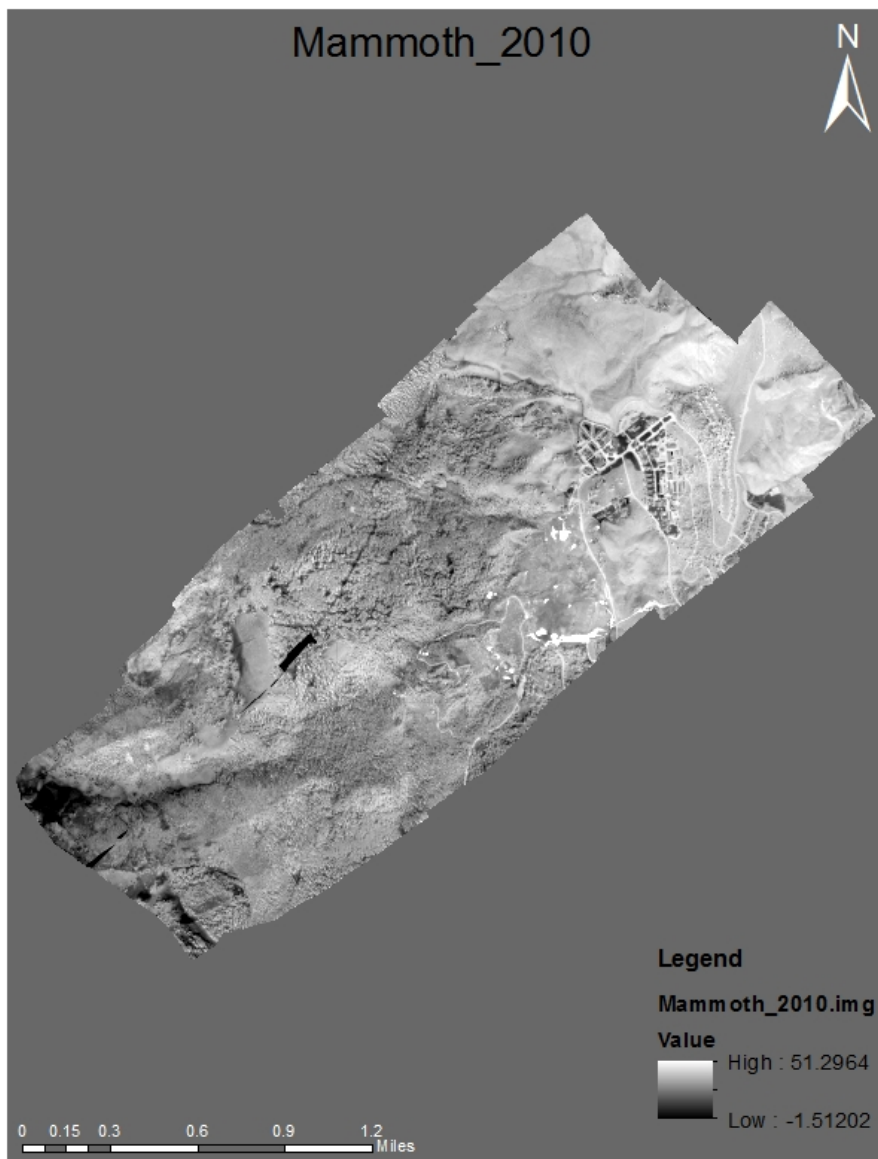
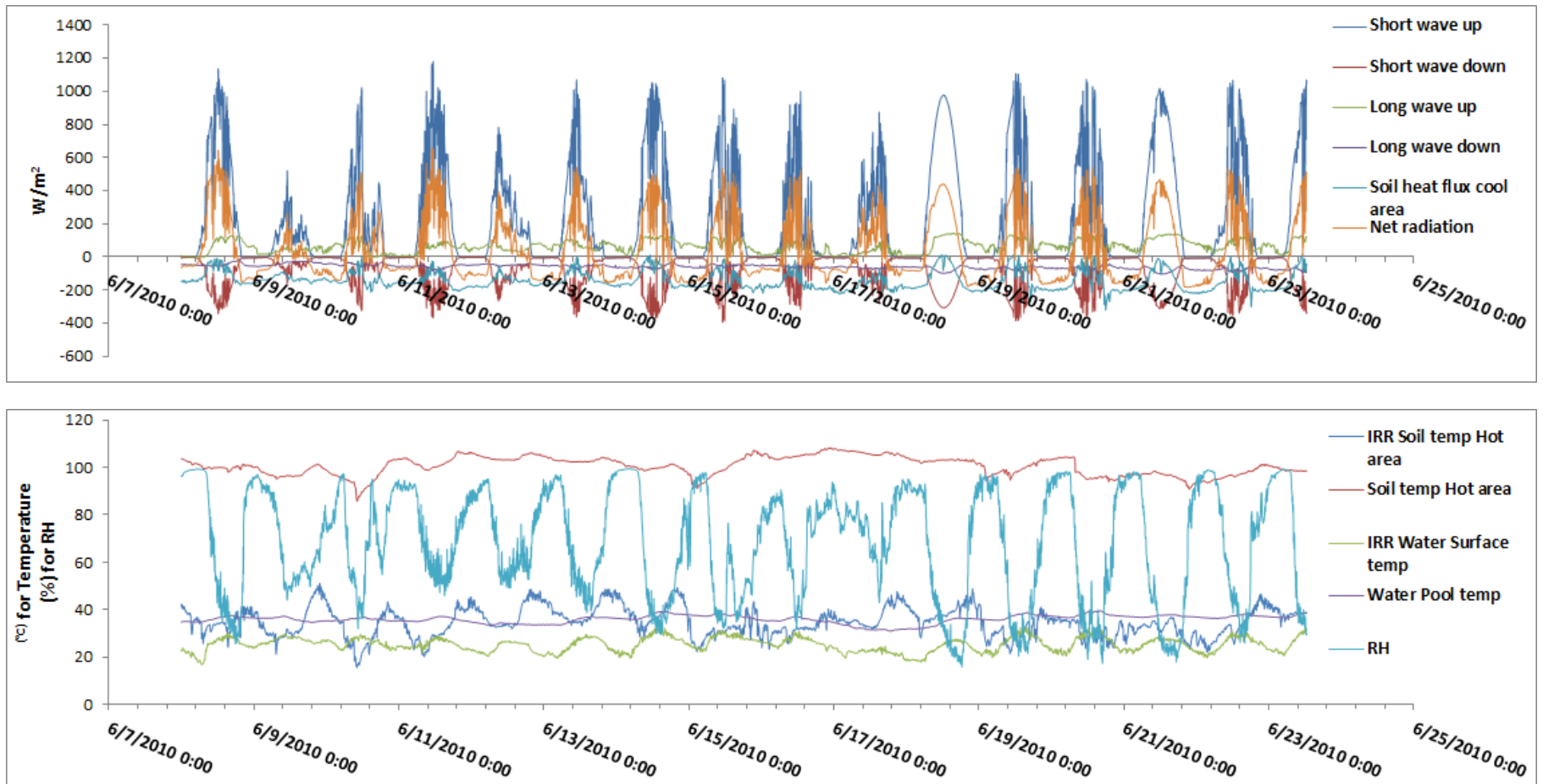


Figure 11. Calibrated and corrected radiometric surface temperature image mosaic for Mammoth Hot Springs acquired in September 2010 and rectified to a LiDAR-based multispectral orthoimage.

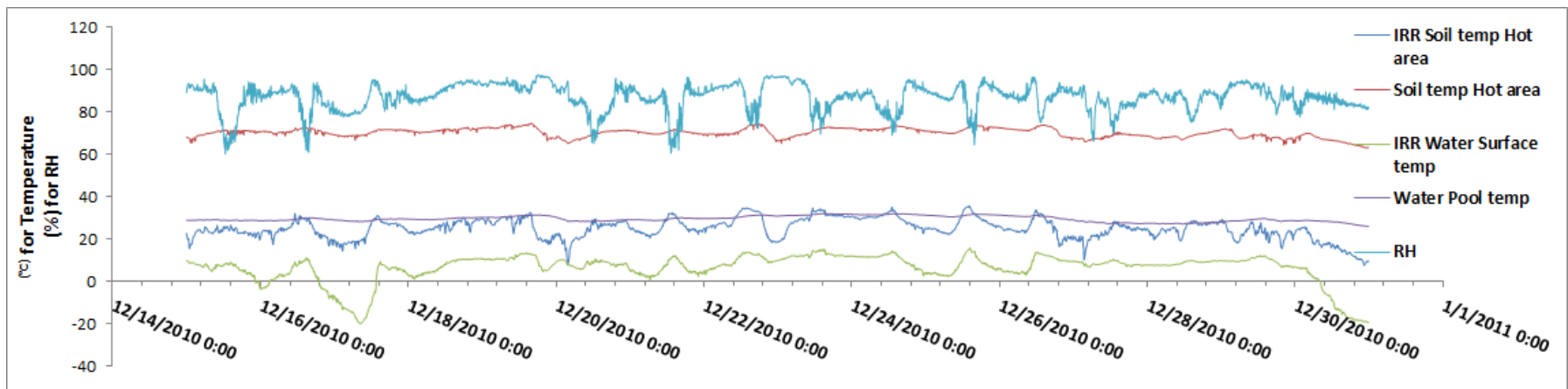
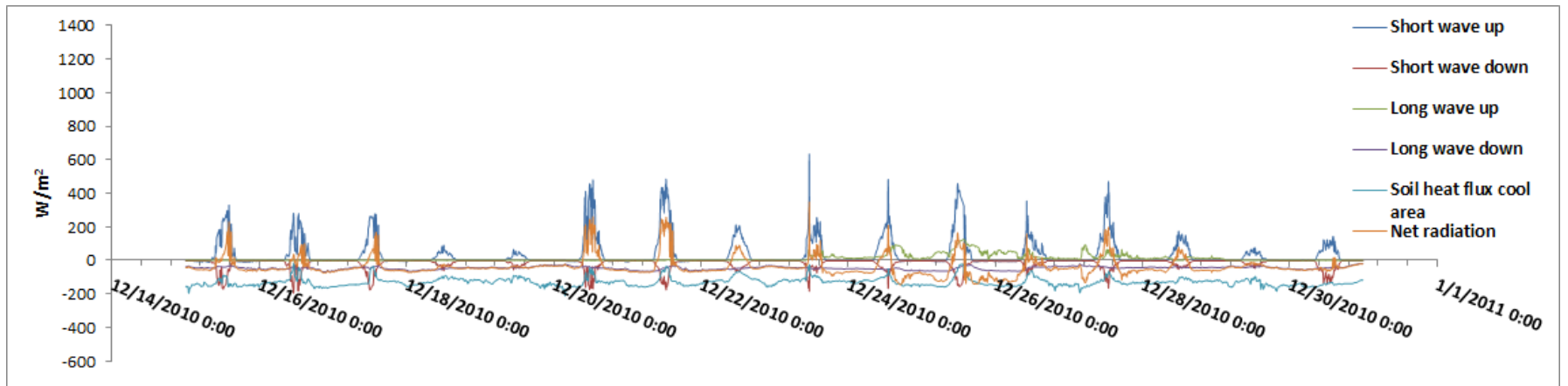
Energy Balance and Heat Flow Experiment at Norris Geyser Basin

As mentioned before, the energy balance experiment had the goal of collecting the data necessary to study the effects of solar heating on the measured airborne thermal infrared surface temperatures. The graphs in Figure 12 show data for a period in the summer of 2010, from Tower #1 (Figure 3). The top graph indicates the radiation balance measured over a geothermal area and the corresponding measured soil heat flux. It can be observed that the soil heat flux is around -170 W/m^2 at night and increases during the day due to a positive down welling contribution from solar heating on the surface. The solar heating effect can also be observed in the daily fluctuations of surface water temperature in the lower graph, measured with the IRR. The wintertime graphs in Figure 13, show a greatly reduced solar heating effect, though on clear days it can still be observed on the IRR measurements of soil and water surface temperatures. Similar patterns can be observed in the graphs from Tower #2 (Figure 4) with very little solar effect in the wintertime (Figures 14 and 15).



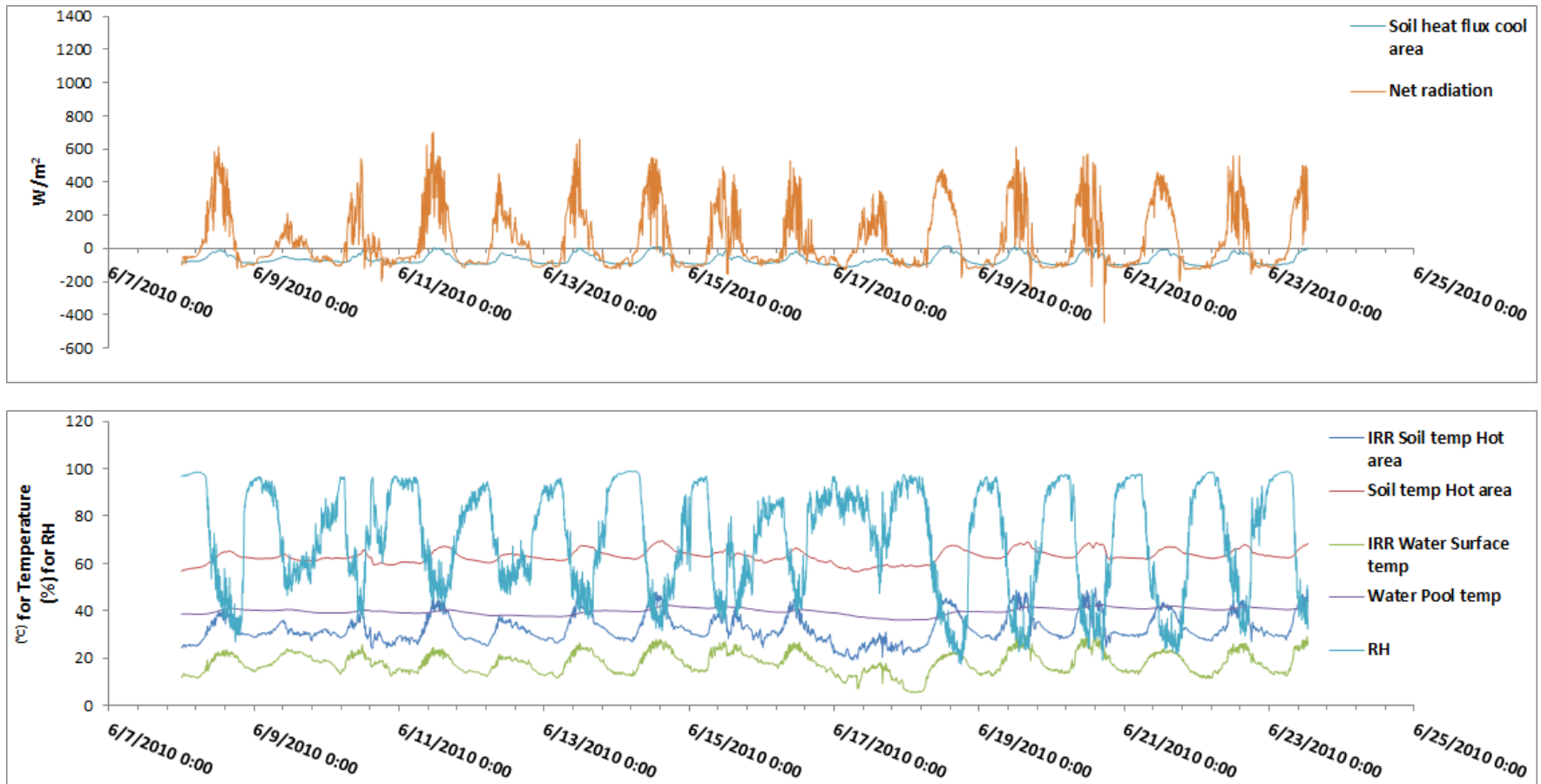
CR3000 - Summer 2010

Figure 12 Sample of measured energy balance data at Tower #1 (Figure 3) showing the radiation balance of shortwave and longwave radiation, net radiation and soil heat flux (top graph) and soil and water surface temperatures (bottom graph) during the summer.



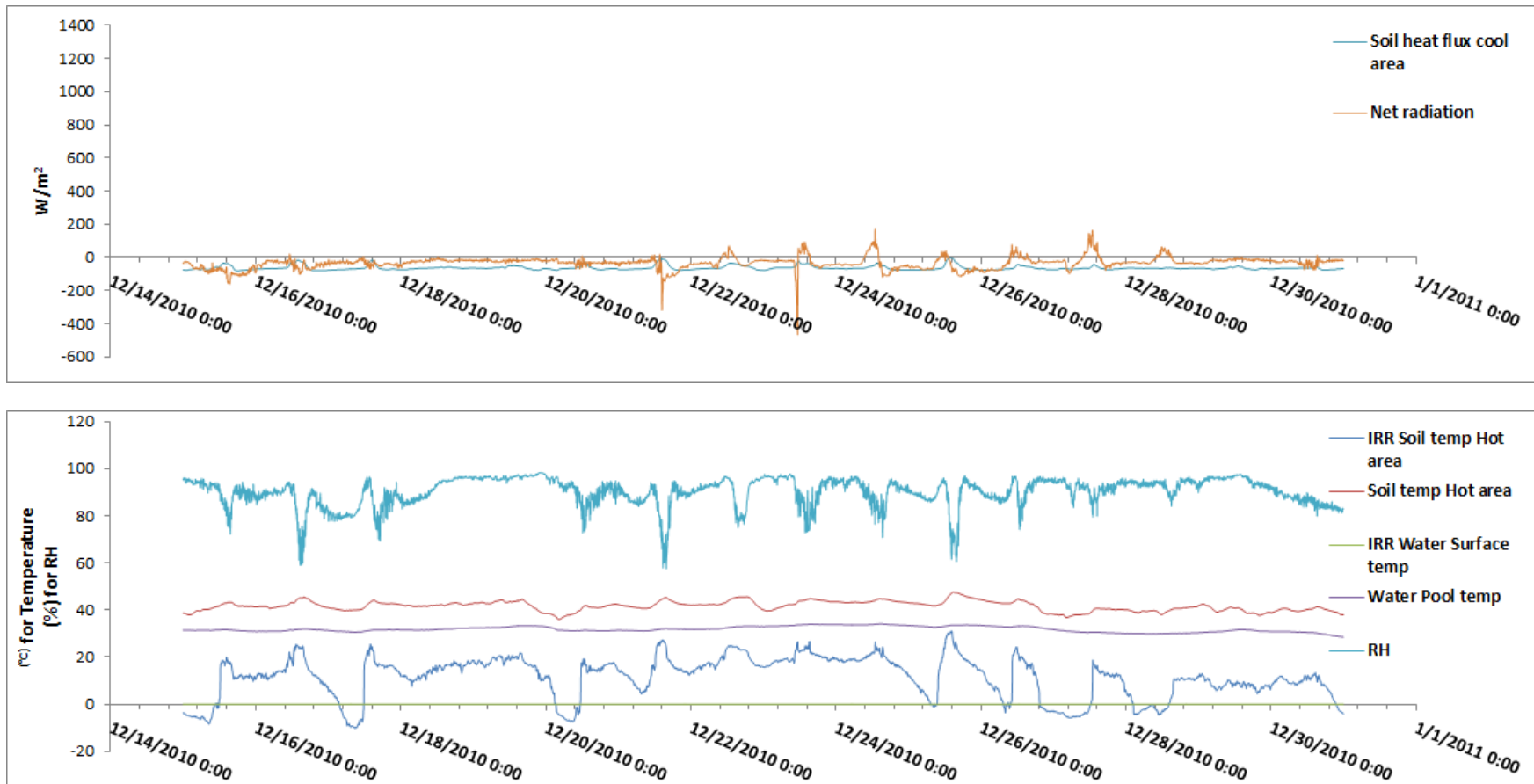
CR3000 - Winter 2010

Figure 13 Sample of measured energy balance data at Tower #1 (Figure 3) showing the radiation balance of shortwave and longwave radiation, net radiation and soil heat flux (top graph) and soil and water surface temperatures (bottom graph) during the winter.



CR1000 - summer 2010

Figure 14 Sample of measured energy balance data at Tower #2 (Figure 4) showing the net radiation and soil heat flux (top graph) and soil and water surface temperature (bottom graph) during the summer.



CR1000 - winter 2010

Figure 15 Sample of measured energy balance data at Tower #2 (Figure 4) showing the net radiation and soil heat flux (top graph) and soil and water surface temperature (bottom graph) during the winter.

One of the objectives of the study is to establish a bulk convective heat transfer coefficient to be used in the heat flow calculations. The following methodology is being applied:

1. Calculation of the Convective Heat Flux at the Ground Surface

The heat flux at the surface (q_{sur}'') in the 'cooler area' within the active geothermal area within the crater is calculated by adding the heat flux measured through the heat flux plate (q'') at 10 cm below the surface to the soil heat storage (S) (eq.1) (Figure 16). The corrected surface temperature (T_s) is calculated with eq. (1.d) using the infrared radiometer (IRR) surface temperature and the emissivity of the sintered soil dominated in that area ($\epsilon \approx 0.9$)

$$q_{sur}'' = q'' + S \quad (1. a)$$

$$S = \frac{\Delta T_s}{\Delta t} \cdot C_s \cdot d \quad (1. b)$$

$$C_s = \rho_b \cdot C_d + \theta_m \cdot C_w \quad (1. c)$$

$$T_s = \sqrt[4]{\frac{IRR^4 - (1 - \epsilon) \cdot T_{background}^4}{\epsilon}} \quad (1. d)$$

where:

d depth (10 cm)

C_s heat capacity of moist soil

ρ_b dry bulk density (1 – 1.6 g cm⁻³)

C_d heat capacity of a dry mineral soil (800 -840 J kg⁻¹ K⁻¹)

θ_m soil water content (measured every 5 minutes)

C_w heat capacity of water =

$$4217.4 - 3.720283 \cdot T_s + 0.1412855 \cdot T_s^2 - 2.654387 \cdot 10^{-5} \cdot T_s^3 + 2.093236 \cdot 10^{-5} \cdot T_s^4 \text{ (J. cm}^{-3} \cdot \text{K}^{-1}\text{)}$$

(Perron & Desnoyers, 1973)

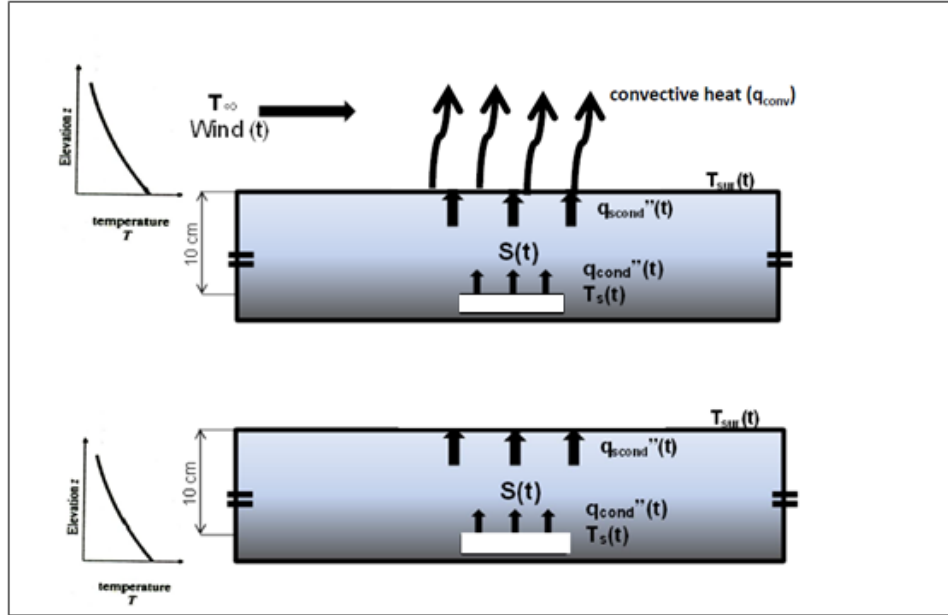


Figure 16: a simulation model of the experiment

2. Decomposition of the Heat Flux Time Series

The heat flux time series is decomposed into three components (seasonal, trend, and random).

$$q_{sur}'' = q_{seasonal}'' + q_{trend}'' + q_{random}'' \quad (2. a)$$

The summation of the seasonal and trend components is used to calculate the heat flux coefficient of the bare soil (h_{soil}) in the cooler area. The random component is used to compare it to soil moisture and wind speed through a regression analysis to determine the correlation.

3. Calculation of the Bulk Convective Heat Coefficient in the Bare Sintered Soil

Summation of the trend and seasonal components of heat flux is used to calculate the bulk convective heat flux coefficient of the bare soil

$$[q_{seasonal}'' + q_{trend}''] = h_{soil} (T_s - T_{atr}) \quad (3. a)$$

$$h_{soil} = \frac{[q_{seasonal}'' + q_{trend}'']}{(T_s - T_{atr})} \quad (3. b)$$

Preliminary results can be seen in Figure 17.

4. Calculation of the Bulk Convective Heat Coefficient of the Water Pool

The explosion crater pool has a dimension of 49m * 44m. The convective heat transfer coefficient of the water pool is calculated through the Nusselt number (N_{ul}), Reynolds number (Re), and Prandtl number (Pr) (eq. 4a, eq. 4b, eq. 4c)

$$N_{ul} = \frac{hL}{k_{air}} = 0.036 Re^{\frac{4}{5}} Pr^{\frac{1}{4}} \quad (4. a)$$

$$Re = \frac{u_{\infty} L \rho}{\mu} \quad (4. b)$$

$$Pr = \frac{\mu/\rho}{\alpha} \quad (4. c)$$

where,

u_{∞} Wind speed (m/s)

L Characteristic length in direction of flow (m) = 49 m

k_{air} thermal conductivity of air (W/m.K)

ρ air density (kg/m³)

μ air viscosity (kg/m.s)

α thermal diffusivity of air (m²/s)

k_{air} , ρ , μ , and α are function of air temperature and pressure.

Statistical Analysis

It is expected that the variability of heat flux estimates is related to soil moisture, wind speed, air temperature and possibly cloud cover. A regression between the random component of the heat flux with wind speed and soil moisture is done to find the correlation. Histograms of the convective heat flux coefficients in bare soil and water pool results were created to determine the values with the highest frequency. Results of this analysis will be written up in a forthcoming journal paper.

Total Heat Flow Calculations

The heat budget above the ground surface is given by the equation:

$$H = \text{Convective Heat} + \text{Radiation Heat} + \text{Mass Transfer Heat} \quad (2.1)$$

Upon estimation of the convective heat coefficients in the bare soil and the water pool from Paper I, we will be able to apply these coefficients spatially using ERDAS IMAGINE to estimate the convective heat power in Norris. The radiation heat will be estimated using Stefan-Boltzmann equation (eq. 2.2)

$$q_{rad} = \epsilon_s \sigma (T_s^4 - T_{\infty}^4) \quad (2.2)$$

where,

ϵ_s surface emissivity (Bare sintered soil = 0.90; Vegetation = 0.98; and water = 0.985)

σ Stefan-Boltzmann constant ($5.67 \times 10^{-8} \text{ W/m}^2/\text{K}^4$)

T_∞ atmosphere temperature = 3 K for clear sky

Mass transfer occurs through latent heat and sensible heat. Latent heat occurs through evaporation and/or condensation in the water surface. Latent heat of vaporization occurs in the summer in wet surfaces, i.e. springs, rivers, water pools, mud pools. In winter, latent heat of fusion occurs through the meltdown of snow or freezing of water particles. In this case, latent heat of vaporization will occur in the snow-covered area as well as in the previously mentioned water surface areas. These components will be estimated and a yearly heat flow budget will be estimated for Norris Geyser basin.

RECOMMENDATIONS

The extraction of the thermal IR images from the sequence files using common and consistent parameters has resulted in a time series of yearly consistent calibrated mosaics that have provided good information for comparative analysis as demonstrated in the journal paper presented in the appendix section of this report that describes the methodology in detail. Future airborne image acquisitions and analysis should follow the same procedures.

The energy balance experiment will provide data that will result in a bulk convective heat flow coefficient that will be used to estimate the convective heat flux from Norris Geyser Basin. These estimates along with radiative and mass transfer heat flux estimates will result in a total heat flow estimation for Norris Geyser basin that can be compared to other methods such as the chloride flux method. Eventually the methodology will be applied to other hydrothermal systems in the park.

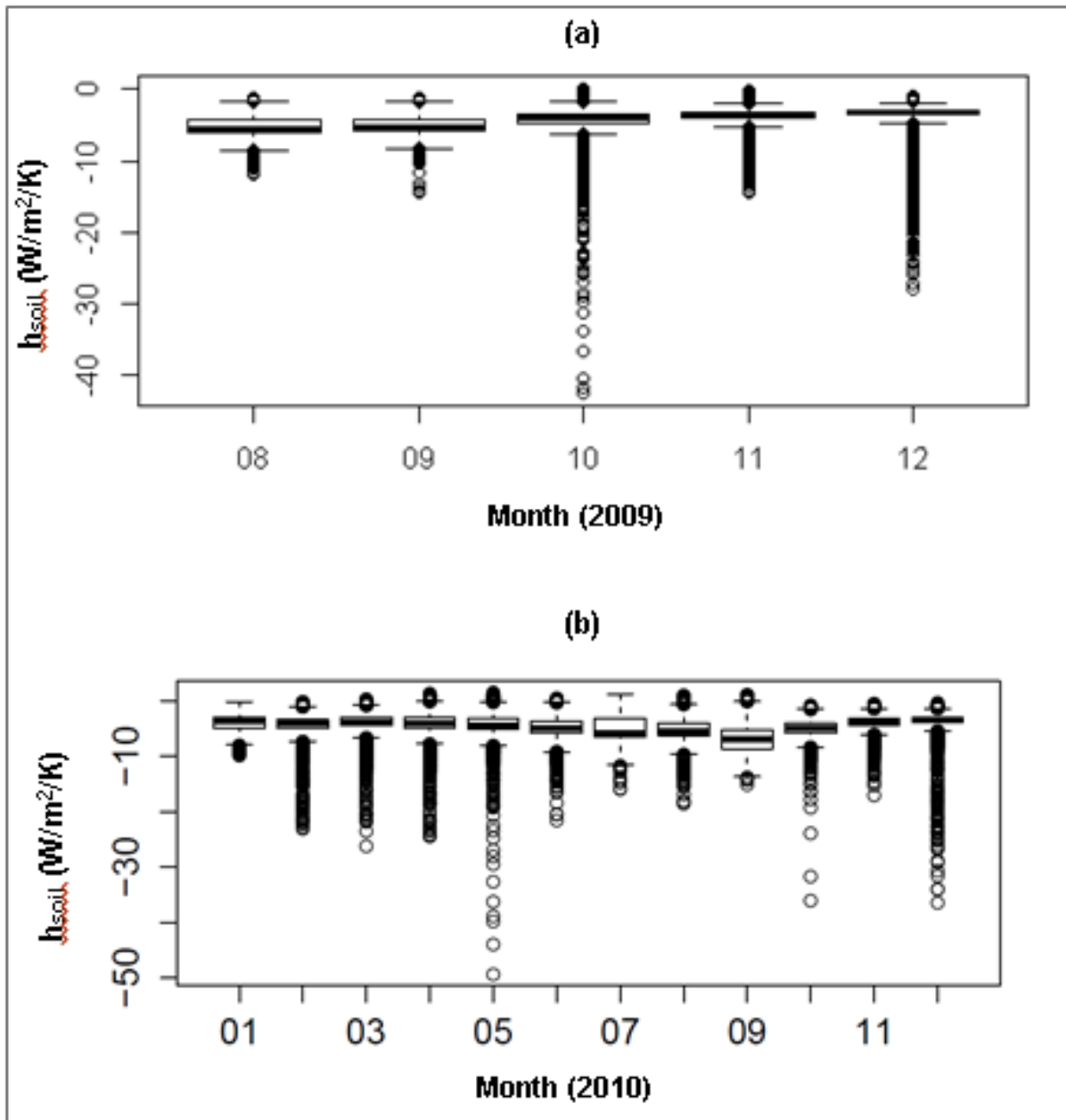


Figure 17: The bulk Convective heat coefficient of the bare soil (h_{soil}) for (a) August-December (2009), (b) January-March (2010). Box plots show the median, 25%, and 75% quartile (contribution from Ruba Mohamed, PhD graduate student)

Additional Sample Products

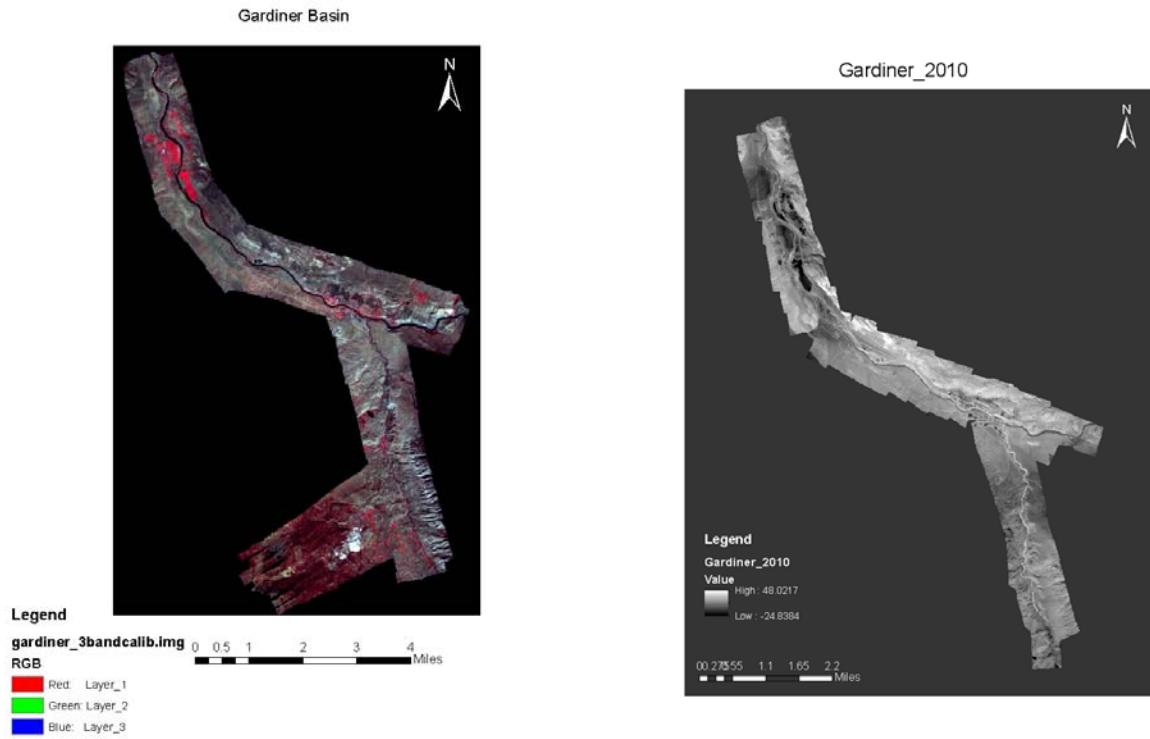
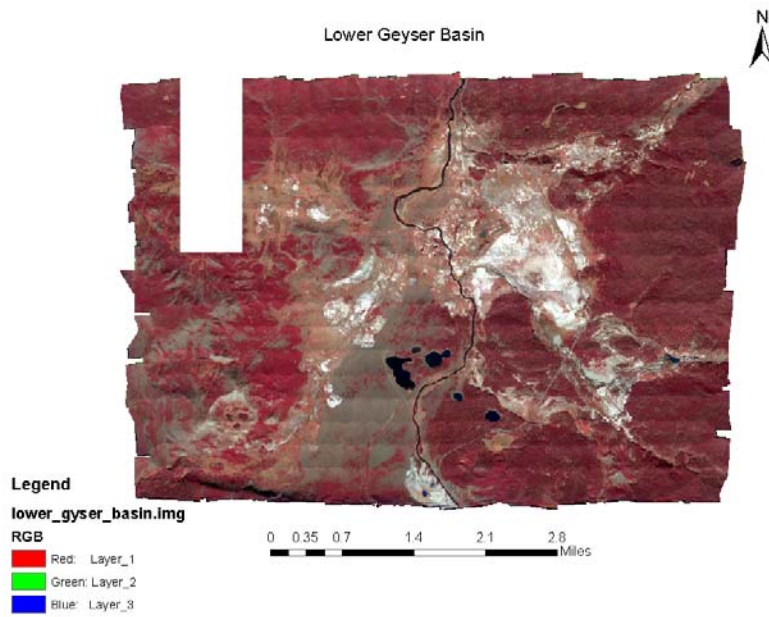


Figure 18 Gardiner River multispectral mosaic and corresponding thermal infrared temperature mosaic



mlb_2010

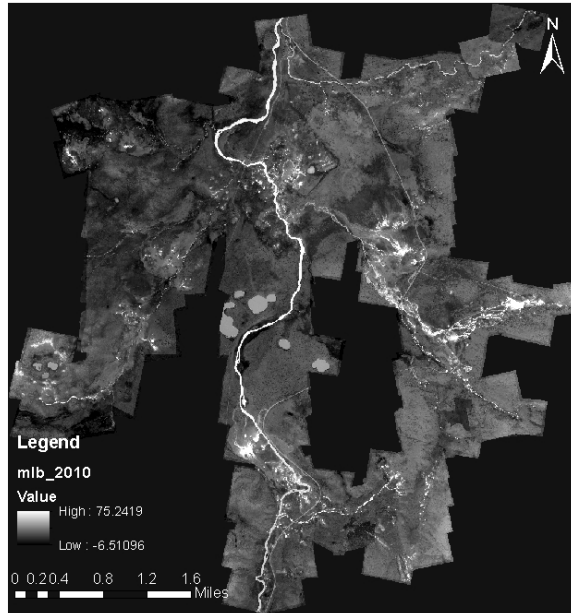


Figure 19 Multispectral and thermal infrared mosaic of the Lower Geyser Basin

REFERENCES

Berk, A., Bernstein, L.S., and Robertson, D.C. "MODTRAN: a moderate resolution model for LOWTRAN 7", Report GL-TR-89-0122. Geophysics Laboratory, Bedford, Maryland, USA. (1989)

Brunsell, N.A., and Gillies, R. "Incorporating Surface Emissivity into a Thermal Atmospheric Correction." Photogrammetric Engineering & Remote Sensing. Vol. 68 (12), pp. 1263-1269 (2002)

Cai, B. and Neale, C. M. U., "A Method for Constructing 3-Dimensional Models from Airborne Imagery" In: Color Photography and Videography for Resource Assessment. Proceedings of the 17th Biennial Workshop. American Society for Photogrammetry and Remote Sensing, Bethesda, MD (1999).

Chávez, J. L., Neale, C. M. U., Hipps, Prueger, J. H. and Kustas, W. P., "Comparing aircraft-based remotely sensed energy balance fluxes with eddy covariance tower data using heat flux source area functions." Journal of Hydrometeorology. Vol. 6, No. 6, 923-940 (2005).

Neale, C.M.U, and Crowther, B., "An airborne multispectral video/radiometer remote sensing system: development and calibration.", Remote Sens. Environ. Vol.49 (3), pp.187-194 (1994)

Quattrochi, D.A and J.C. Luvall, [Thermal Remote Sensing in Land Surface Processes], CRC Press, Boca Raton, Florida (2003).

Sundararaman, S. and Neale, C. M. U. , "Geometric Calibration of the USU Videography System", In: Videography and Color Photography for Resource Assessment. Proceedings of the 16th Biennial Workshop. American Society for Photogrammetry and Remote Sensing, Bethesda, MD. (1997)

Torgersen, C.E., Faux, R.N., McIntosh, B.A., Poage, N.J., and D.J. Norton. "Airborne thermal remote sensing for water temperature assessment in rivers and streams." Remote Sensing of Environment. Vol. 76, 386-398 (2001).

APPENDICES

A. Journal Paper

1 **HYDROTHERMAL MONITORING IN YELLOWSTONE NATIONAL PARK USING**
2 **AIRBORNE THERMAL INFRARED REMOTE SENSING**
3

4 CMU Neale^{*a}, C. Jaworowski^b, H. Heasler^b, S. Sivarajan^{a,c}, and A. Masih^a

5
6 ^a Remote Sensing Services Laboratory, Civil and Environmental Engineering Dept., Utah State
7 University, Logan, UT 84322, USA;

8 E-Mail: christopher.neale@usu.edu; masih.ashish@gmail.com

9 ^b Yellowstone Center For Resources, Yellowstone National Park, WY 82190, USA,

10 E-Mail: cheryl_jaworowski@nps.gov, henry_heasler@nps.gov
11

12 **ABSTRACT**

13
14 Acquisitions of thermal infrared (8-12 μm) images for two active hydrothermal areas in
15 Yellowstone National Park utilized the Utah State University multispectral airborne system and a
16 FLIR SC640 thermal infrared camera. Thermal infrared image acquisitions under clear-sky
17 conditions after midnight met the objective of providing high-spatial resolution, georectified
18 thermal infrared imagery for select hydrothermal systems. This paper describes the image
19 acquisition and processing methodology, including surface emissivity and atmospheric
20 corrections, for generating at-surface ground temperatures. Comparison of corrected radiative
21 temperature maps with measured ground and water surface kinetic temperatures at flight times
22 provided an assessment of temperature accuracy. A repeatable time-series of September images
23 for the Hot Spring Basin and Norris Geyser Basin hydrothermal systems demonstrated that the
24 technique can generate night-time, thermal infrared imagery for documentation of variable
25 temperatures and fluid flow.

26
27 **Keywords:** Airborne thermal infrared remote sensing, hydrothermal systems, emissivity,
28 Yellowstone

* cneale@nebraska.edu ; phone +1 402 4725145 fax +1 402 4729545, Presently at Daugherty Water for Food
Institute, University of Nebraska, Whittier Research Building 234B, 2200 Vine St, Lincoln, NE 68583

^c Presently at Agricultural and Biosystems Engineering, North Dakota State University, Fargo, ND 58108, USA; E-
Mail: saravanan.sivarajan@ndsu.edu

29

30 **1.0 INTRODUCTION**

31 Protection of Yellowstone National Park’s hydrothermal systems involves the utilization
32 of rigorous scientific information and knowledge of the geologic processes responsible for their
33 occurrence. Established in 1872, Yellowstone National Park is famous for its globally rare
34 collection of hydrothermal features - geysers, mud pots, steam vents, and hot springs. An
35 unusual heat source, cold groundwater recharge, and a natural network of fluid flow pathways
36 are necessary for these composite natural resources - hydrothermal features and the hydrothermal
37 system. The U.S. Congress requires the monitoring of Yellowstone’s hydrothermal system.

38 Beginning in 2007, an airborne thermal infrared monitoring technique gathered night-
39 time baseline data for hydrothermal systems within Yellowstone National Park (YNP) using a
40 state-of-the-art FLIR SC640, broad-band (8-12 micron) thermal infrared (TIR) camera flown at
41 1,800 m (6,000 ft) above ground level. Airborne image acquisition campaigns occurred during
42 night-time in September and yielded uncorrected temperature images with 1-m spatial resolution.
43 Fall acquisitions minimized solar heating effects and the cooling of the ground associated with
44 snowmelt. Calibration and corrections for atmospheric effects in the imagery as well as
45 emissivity of the ground generated temperature maps of the two hydrothermal systems.
46 Comparison of derived radiative temperatures with ground temperatures of hydrothermal pools
47 provided an assessment of the monitoring technique’s thermal accuracy for various temperatures.

48 Remote sensing techniques proved an effective means to monitor the Park’s
49 hydrothermal systems. The ideal goal of such a remote sensing technique is TIR night-time
50 imagery with 1-m spatial resolution and 1°C temperature accuracy. Although satellite imagery
51 (Landsat, ASTER and MODIS) covers large areas effectively, the spatial resolution is too coarse
52 (60 to 1000 meters) for the stated goals.

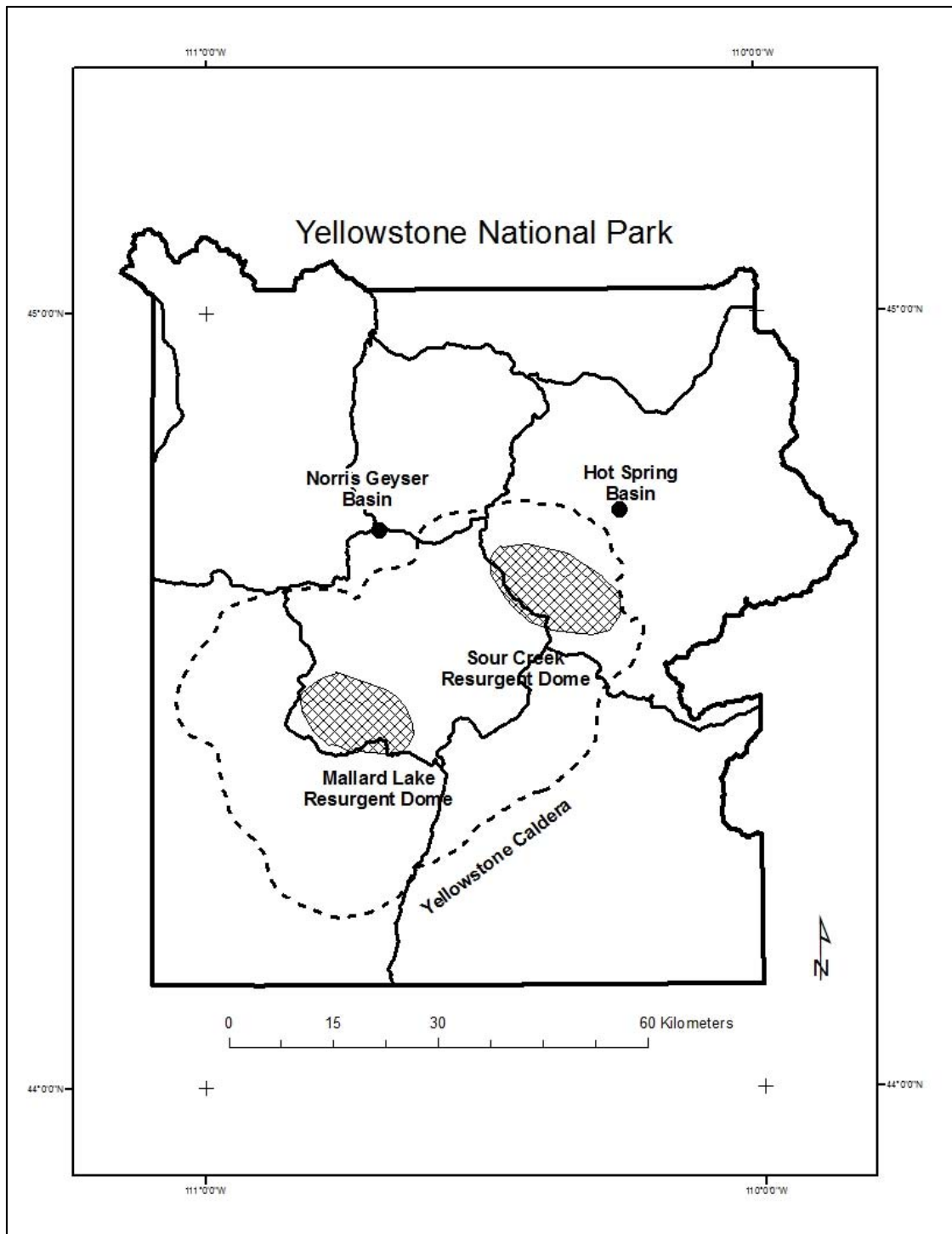
53 Satellite-based remote sensing in the TIR part of the spectrum estimated surface energy
54 balance components and evapotranspiration over large agricultural areas (Bastiaanssen et al.
55 1998, Kustas and Norman, 1999, Li et al, 2005, Taghvaeian and Neale, 2012) and monitored
56 urban areas (Roberts et al. 2012). Other satellite studies modeled Yellowstone's snow-free areas
57 with LANDSAT (Watson and others, 2008), used LANDSAT summer imagery for park wide
58 monitoring of geothermal areas (Savage and others, 2010) or used night-time ASTER and
59 MODIS imagery for monitoring geothermal activity and estimated a park-wide radiant
60 geothermal heat flow (Vaughan and others, 2012). A recent literature review (Li et al. 2013)
61 highlighted the challenges in extracting land surface temperatures from satellite sensors.
62 Previous airborne remote sensing applications involved assessing water temperatures in rivers
63 and streams (Torgesen et al, 2001) and estimating surface parameters (Quattrochi and Luvall,
64 2003).

65 For decades, Yellowstone National Park has been a test bed for airborne sensors and
66 applied work. Early remote sensing work focused airborne TIR and radar sensors on geologic
67 applications (Christiansen, 1966; Keefer, 1968; Pierce, 1968; Prostka, 1966; Ruppel, 1966;
68 Smedes, 1968). These early airborne TIR sensors used a broad band 3 to 5 μm sensor. Airborne
69 TIR studies still use a broad band 3 to 5 μm sensor and broad band or split-channel 8 to 12 μm
70 sensors (Hardy, 2005; Seielstad and Queen, 2009). Hardy (2005) focused his doctoral research
71 on TIR but also utilized multi-spectral visible, near-infrared (NIR) and a previously flown
72 hyperspectral data set (Livo and others 1999). This doctoral work on airborne TIR remote
73 sensing influenced the National Rocky Mountain Cooperative Ecological Study (RM-CESU) by
74 Seielstad and Queen (2009). They evaluated monitoring methods, provided baseline data for
75 selected geothermal systems, and produced an initial heat estimate for Norris Geyser Basin. The

76 studies by Seielstad and Queen (2009) set the stage for the airborne, night-time RM-CESU
77 thermal infrared studies by the Neale and others (2011) within Yellowstone National Park.
78 Other relevant studies of ground and airborne TIR by Bayani and others (2011) and Jaworowski
79 and others (2012) utilized a single channel 8-12 μm sensor to investigate hydrothermal fluid flow
80 within Midway Geyser Basin and the Upper Geyser Basin hydrothermal system, respectively.
81 Thus, a time-series of airborne, night-time, TIR imagery now exists for selected hydrothermal
82 systems within Yellowstone National Park.

83 This paper describes the TIR monitoring technique used for acquiring and processing
84 baseline imagery and presents results for two hydrothermal systems: Hot Spring Basin (HSB)
85 and Norris Geyser Basin (NGB) (Figure 1). The time series for HSB covers the 2007 to 2011
86 period whereas the time-series for NGB spans the 2008 to 2011 period. Hydrothermal fluid flow
87 in both natural systems is the result of permeable pathways within the 640,000 Lava Creek Tuff.
88 Although HSB is acid-sulfate system and NGB has acid sulfate and neutral chloride
89 hydrothermal features, both hydrothermal systems occur outside the 640,000 year old
90 Yellowstone caldera. The main goal of this research is the development of a repeatable
91 methodology for monitoring the Yellowstone hydrothermal system and documenting the
92 system's variable temperature and hydrothermal fluid flow.

93



94
 95 **Figure1.** Map showing location of the Norris Geyser Basin and Hot Spring Basin hydrothermal
 96 systems (black dots) within Yellowstone National Park. The map also highlights major roads
 97 (solid black lines), the 640,000 Yellowstone caldera (black dashed line) and two resurgent domes
 98 (Mallard Lake and Sour Creek; cross-hatched areas). Geologic data from Christiansen (2001)
 99 and other digital information from NPS Data Store (http://www.nps.gov/gis/data_info/).

100 **2.0 METHODS**

101 The Utah State University (USU) airborne remote sensing system, image acquisition, and
102 image processing for multispectral (MS) and thermal infrared (TIR) systems is the focus of the
103 METHODS section of this paper. Discussion of the geo-rectification and image processing
104 procedures for daytime visible and nighttime thermal infrared images within these hydrothermal
105 areas provides necessary information for the generated products. Image calibration, corrections
106 for lens effects, mosaicking of individual images and atmospheric corrections of at-aircraft
107 temperatures as well as emissivity corrections for soil, vegetation, earth and water generated
108 corrected temperature mosaics useful for assessment of hydrothermal systems.

109

110 **2.1 Utah State University Airborne Remote Sensing System**

111 The USU airborne MS digital system used on this project between 2007 and 2010 has
112 three Kodak Megaplug 4.2i Digital Cameras with imaging sensors producing images with
113 approximately 2000 x 2000 pixels (Cai and Neale, 1999). The Nikon 20 mm lenses have
114 interference filters forming spectral bands centered in the green (0.55 μm), red (0.67 μm) and
115 near-infrared (0.8 μm) portions of the electromagnetic spectrum. A porthole in the belly of a
116 Cessna TU206 single engine aircraft, dedicated to remote sensing (Figure 2) held the cameras
117 within a high-grade aluminum/carbon composite mount. A FLIR SC640 camera with a 40 mm
118 lens mounted through a different porthole and aligned with the MS system cameras (Figure 2c)
119 acquires thermal infrared imagery in the 8 to 12 μm range. Boards and software installed in a
120 fast PC computer with two 500 GB hard drives for storage of the imagery controlled both the
121 digital and TIR cameras. Since 2007, the USU airborne MS digital system and TIR imager

122 (FLIR SC640) have been used in numerous applications that require high-spatial resolution
123 imagery (Neale et al, 2012, Geli et al, 2012).

124 In 2010, USU developed an integrated airborne MS system and Lidar Assisted Stereo
125 Imager (LASSI) LIght Detection And Ranging (LiDAR) system. The LiDAR system has a full-
126 waveform Riegl Q560 LiDAR transceiver, and a Novatel SPAN LN-200 Global positioning
127 system (GPS)/inertial measurement unit (IMU) Navigation System. The LiDAR is capable of
128 working up to 1200 m (4000 ft) above ground level (AGL), but for this project the aircraft flew
129 at 700 m (2296 ft). Given the pulse rate of 100,000 shots per second, a flight speed of 185 km/h
130 (110 mi/h) and a scan rate of 75 Hz, the result is an average shot density of 2.1 shots per square
131 meter within a given strip. In overlap areas, this density is 2 to 3 times greater, so due to a 50%
132 side-lap specification, an average shot return of greater than 2 shots per square meter was
133 obtained. The LiDAR has beam divergence of less than 0.5 m_rrad and therefore has a footprint
134 size of about 0.5 m at 1000 m (3300 ft) AGL. Digitized at a rate of 1 GHz, the waveform for
135 each shot yielded a volume spacing of 0.3 m for each single shot within the vegetation.

136 Additional processing of this waveform produced multiple points per laser shot. Four ImperX
137 Bobcat cameras with 4904 x 3280 pixel density sensors, with interference filters forming spectral
138 bands in the Blue (0.465-0.475 μm), Green (0.545-0.555 μm), Red (0.645-0.655 μm) and Near
139 Infrared (NIR) (0.780-0.820 μm) acquired the MS images for the new system. Using the
140 Terrascan and Terraphoto/Microstation software, data from the IMU system, Lidar point cloud-
141 based Triangular Irregular Networks (TINS), and the time stamped images, rectified orthoimages
142 are produced through direct georeferencing.

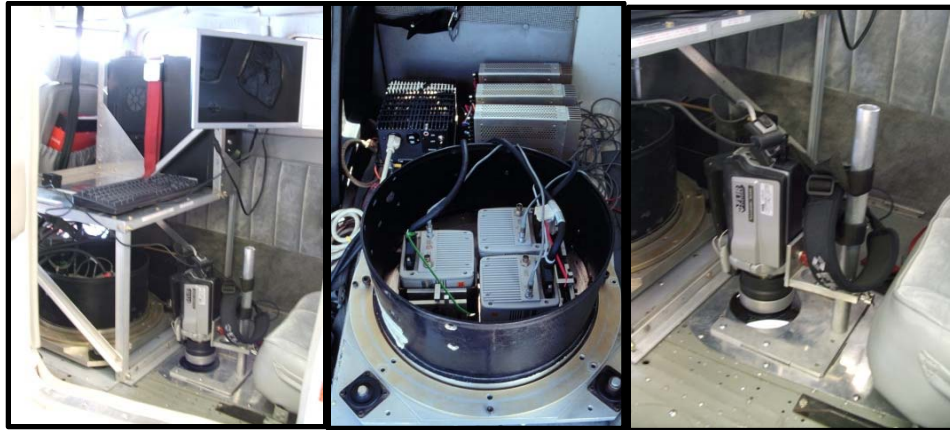
143

144

(a)

(b)

(c)



145

146

(d)

(e)



147

148 **Figure 2.** (a) The USU airborne multispectral (MSS) remote sensing system installed in the
149 Cessna TP206; (b) the Kodak Megaplug 4.2i camera; (c) the FLIR SC640 thermal IR camera;
150 (d) the LASSI integrated LiDAR/multispectral system and (e) view of the installed integrated
151 system from below.

152

153 2.2 Image Acquisition

154 Image acquisitions for YNP occurred during the month of September, a typically dry
155 month with clear-sky conditions and little significant fall/winter snow accumulation. During that
156 time of the year, the air temperature drops significantly after sunset at the high altitudes of
157 Yellowstone Park (averaging 2400 m; 8000 ft) and the surface temperature drops to around or

158 below freezing due to radiative cooling, allowing for good temperature contrast between
159 hydrothermal areas and surrounding cooler areas. The night-time TIR image acquisition flights
160 planned after 11:00 p.m. typically lasted 3 to 4 hours. While the coldest air and surface
161 temperatures typically happened close to sunrise, the team avoided flying at that time due to the
162 formation of dew and increased water vapor occurring over and around the hydrothermal pools.
163 Therefore, the acquisition minimized the masking effect of water vapor on high temperature
164 pools and resulting errors in surface radiometric temperature estimation.

165 The monitoring effort involved image acquisition of high-priority hydrothermal areas
166 such as Norris Geyser Basin, and Hot Spring Basin. The flight lines provided an overlap of 30%
167 among images in parallel lines. The FLIR SC640 camera has a sensor with 640 x 480 pixels.
168 Determining appropriate flight altitude is essential for acquiring 1-m pixel resolution images
169 with the 40 degree field-of-view camera lens. Typically, the aircraft is flying 1800 meters (6000
170 feet) above ground level (AGL) for safe nighttime flying, well above the mountains. The
171 ThermoVison ExaminIR, version 1.10.2 software controlled the FLIR camera. Capture of digital
172 images happened at a frequency of 5 frames a second and storage of digital images was in
173 sequential (SEQ) digital format. Prior to acquiring the first images, the aircraft flew down the
174 center of the hydrothermal area so that the lens focus guaranteed crisp, high-spatial resolution
175 thermal IR images. The FLIR SC640 camera acquires imagery in the -40 to 120 °C range.

176 A typical September image acquisition may include a single daytime flight over any new
177 area to obtain shortwave 3-band MS imagery and sometimes LiDAR and a nighttime flight for
178 thermal IR imagery. The day flights take place between solar noon and mid-afternoon under
179 clear skies, usually the hottest time of the day. The daytime MS images (1-m pixel resolution)
180 form the calibrated 3-band orthomosaics that serve as image base maps for rectification of the

181 nighttime TIR imagery. When the LiDAR is in use, the aircraft flies at around 700-800 m (2300
182 to 2600 ft) AGL, resulting in higher resolution MS imagery varying from 0.2 to 0.4 m pixel
183 sizes.

184

185 **2.3 Image Processing**

186 Correcting the MS images for lens vignetting effects (Neale and Crowther, 1984) and for
187 lens radial distortions (Sundararaman and Neale, 1999) and registering 3-band images for geo-
188 rectification were the initial steps. Between 2007 and 2009, a digital color-IR orthophotographic
189 imagery produced by the Wyoming Geographic Advisory Committee
190 (<http://www.uwyo.edu/wygisc/>) and common well-defined control points (pixels) formed the
191 image base. Rectifying the USU airborne MS images to the georectified base map involved a 3rd
192 order polynomial transformation. The root mean square error (RMSE) error for the individual
193 image rectification was kept to less than 1-m. Assembling the image strips involved sub-setting
194 and mosaicking of rectified images along the flight lines. Calibration of these image strips to a
195 reflectance standard involved using the system calibration through a similar procedure described
196 by Neale and Crowther (1994). A standard reflectance panel with known bi-directional
197 properties (Jackson et al, 1984) was set up in a central location during the flight, overlooked
198 from nadir by an Exotech radiometer with Thematic Mapper bands (similar to the airborne
199 digital cameras). The radiometer measured incoming irradiance from the sun and sky every
200 minute, which was then used to calibrate the image strips in terms of reflectance. The location of
201 the standard reflectance panel setup was either at the Old Faithful area in Yellowstone National
202 Park or at the West Yellowstone, Montana, airport. Once calibrated, stitching the rectified image
203 strips together produced a mosaic for each hydrothermal area. The calibrated, 3-band

204 orthomosaics formed the base map for rectification of the night-time TIR imagery and used for
205 emissivity corrections.

206 Prior to image processing, extraction of individual TIR images from the native format
207 SEQ files at approximately 60 to 70 % overlap along the flight line is necessary. Standardization
208 of the image extraction procedure using the ExaminIR software, included setting variables and
209 parameters the same for all flights: the emissivity is set to 1, the background air temperature to 0°
210 C with a relative humidity of 10%, and a temperature of the external optics of 10° C and
211 transmissivity of 1

212 Visual rectification of the individual TIR images to the 3-band MS orthomosaic involved
213 the use of common ground control points. Stitching individual TIR images together along the
214 flight lines created the night-time TIR image strips. The formation of a nighttime TIR mosaic
215 for a hydrothermal area entailed the mosaicking of several calibrated strips from parallel flight
216 lines.

217 Correction of the at-aircraft temperature image mosaics for atmospheric transmission
218 effects included the application of the MODTRAN (MODerate resolution TRANsmission)
219 radiative transfer model (Berk et al, 1989). Radiosonde data collected in Great Falls, MT at 0
220 and 12 GMT provided the profile of temperature and humidity between the surface and the
221 aircraft altitude, required as input data by the model. Because Great Falls is at lower elevation
222 than the hydrothermal areas in YNP, only the portion of the profile starting at the corresponding
223 elevation and anchored with the dew point temperature data from local surface weather stations
224 within the Park was necessary. MODTRAN was run multiple times for the atmospheric profile
225 and for different surface emissivity, ranging between 0.90 and 0.98. A regression line enabled

226 the adjustment of airborne radiometric temperatures in the image according to surface emissivity
227 and the atmospheric profile at the time of the flight.

228 The technique proposed by Brunsell and Gillies (2002) afforded an estimate of surface
229 emissivity. The scaled Normalized Difference Vegetation Index (NDVI) obtained from the
230 calibrated 3-band image mosaic yielded a fraction of vegetation cover layer for linear scaling the
231 emissivity of the surface between bare sintered soil (0.90), and full canopy /dense vegetation
232 cover (0.98). The ERDAS Imagine software processed all imagery. The application of the
233 Normalized Difference Vegetation Index (NDVI) to the calibrated 3-band image mosaic for
234 generation of image layer utilized the following equation:

$$235 \quad \text{NDVI} = (\text{NIR} - \text{Red}) / (\text{NIR} + \text{Red}) \quad (1)$$

236 Scaling the NDVI yielded the N* parameter in raster form:

$$237 \quad \text{N}^* = (\text{NDVI} - \text{NDVI}_0) / (\text{NDVI}_{\text{max}} - \text{NDVI}_0) \quad (2)$$

238 Where NDVI₀ is the bare soil NDVI value of the scene and NDVI_{max} is the maximum NDVI of
239 the scene corresponding to full cover dense vegetation. The fraction of vegetation cover (Fr)
240 became:

$$241 \quad \text{Fr} = \text{N}^{*2} \quad (3)$$

242 Linear scaling the emissivity between bare sintered soil ($\epsilon_{\text{soil}} = 0.90$) and full dense vegetation
243 cover ($\epsilon_{\text{veg}} = 0.98$) using the Fr image layer produced the surface emissivity layer:

$$244 \quad \epsilon_{\text{surf}} = \text{Fr} (\epsilon_{\text{veg}}) + (1 - \text{Fr}) \epsilon_{\text{soil}} \quad (4)$$

245 Applying equations 1 through 4 to the calibrated MS 3-band mosaic, using the at-aircraft
246 radiometric temperature mosaic and the developed temperature correction from MODTRAN, an
247 ERDAS Imagine model generated a spatial surface emissivity layer. Assigning an emissivity of
248 0.985 to water surfaces in the scene involved the identification of water using spectral

249 classification of the high-resolution calibrated 3-band image to produce a spatial water body
250 mask. The model output is an at-surface radiometric temperature image layer corrected for
251 atmospheric effects and surface emissivity.

252

253 **3.0 ASSESSMENT OF THERMAL INFRARED TECHNIQUE**

254 For Norris Geyser Basin and Hot Spring Basin, temperature data provided an assessment
255 of the TIR technique's precision and accuracy. A comparison of the highest radiative
256 temperature for all years of image acquisition is a measure of the estimated radiative
257 temperatures for both hydrothermal systems. At Norris Geyser Basin, the accessibility of this
258 hydrothermal system enabled a comparison of measured ground and pool kinetic temperatures
259 with the calculated radiative temperatures. Additionally, a qualitative assessment of spatial
260 accuracy for Norris Geyser Basin offered useful information for geologic applications and
261 scientific visualizations.

262

263 **3.1 Consistency of Calculated Radiometric Temperatures**

264 The maximum, radiative temperature within the corrected TIR images is an indication of
265 consistency of the night TIR image acquisition. At different dates and times, the highest
266 temperatures of a hydrothermal system should approach 90 to 92°C- the boiling temperature of
267 water at the average elevation (2,400 m) of Yellowstone. It is reasonable that the corrected,
268 airborne TIR temperatures are less than the maximum kinetic temperatures because water vapor
269 masks the true surface temperatures of hydrothermal ground or pools. However, the maximum
270 radiative temperatures derived from the TIR imagery should be internally consistent due to the
271 presence of water vapor above the hottest pools.

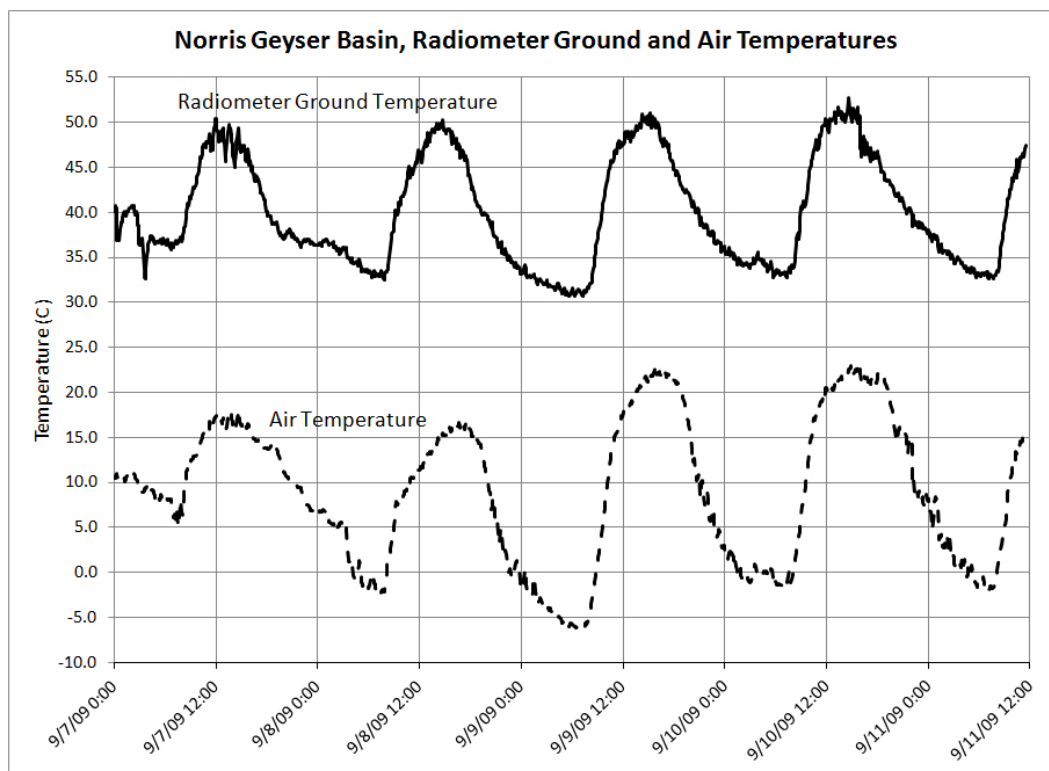
272 A summary of basic image information (Table 1) for the two hydrothermal systems- Hot
273 Spring and Norris Geyser basins-highlights the date/time of night-time TIR image acquisitions
274 and the air temperature near ground level for 2007 through 2011. The meteorological station
275 located at the Lake Water Tank (<http://ard-request.air-resource.com>) provided air temperatures
276 for the Hot Spring Basin comparison and a YNP Geology Program Onset temperature logger at
277 the Norris Museum for Norris Geyser Basin provided air temperatures for the Norris Geyser
278 Basin assessment. For Hot Spring Basin TIR imagery, the maximum radiative temperature
279 (Table 1) is 67.4 °C with a standard deviation of 1.4 °C. For Norris Geyser Basin TIR imagery,
280 the maximum radiative temperature is 69.4 °C with a standard deviation of 3.8 °C. Not
281 surprisingly, atmospheric conditions were not identical from year to year and the air
282 temperatures at the time of the flight indicate this variability.

283 Fluctuations in radiometric ground temperature demonstrate that the time of the 2009
284 night TIR flight occurred near the minimum residual solar heating (Figure 3). At Norris Geyser
285 Basin, a hydrothermal explosion crater contained an experiment for measuring the variable
286 residual solar heating (Figure 4). An infrared radiometer mounted on a pole and pointing at hot,
287 dry thermal ground measured the daily fluctuations during the 10 September 2009 image
288 acquisition. The ground surface temperatures reached a minimum around 6:00 a.m., close to the
289 minimum air temperature, and then increased after sunrise reaching a peak around 2:00 p.m.
290 Flights typically occurred between midnight and 4:00 a.m. with low ground surface temperatures
291 (Table 1), varying between 2 to 4 °C above the minimum temperature. The amount of solar
292 heating and radiative cooling varied according to atmospheric conditions during the previous
293 day, cloud cover, precipitation, and air temperature. Future investigations will address and
294 correct for this known effect within the airborne, radiative temperature images.

295 **Table 1.** Calibrated image mosaics statistics for several flights over Hot Spring Basin and Norris
 296 Geyser Basin.

Area	Date	Time (a.m.)	Maximum Temperature	Air Temperature	Air Temperature Source
Hot Spring Basin					
2007	9/13	12:06-12:19	66.73 °C	0.9°C	NPS Lake-WT
2008	9/12	11:52-12:13	68.14 °C	2.6 °C	NPS Lake-WT
2009	9/10	1:17-1:37	69.37 °C	8.3°C	NPS Lake-WT
2010	9/25	11:45-12:04	67.24 °C	6.6°C	NPS Lake-WT
2011	9/8	1:22-1:42	65.69 °C	6.9°C	NPS Lake-WT
Norris Geyser Basin					
2008	9/12	1:31-1:53	69.47 °C	-0.6 °C	Norris Museum
2009	9/10	3:36-3:53	72.77 °C	2.5 °C	Norris Museum
2010	9/25	12:33-12:49	71.30 °C	4.2 °C	Norris Museum
2011	9/9	12:08-12:31	64.08 °C	5.8 °C	Norris Museum

297

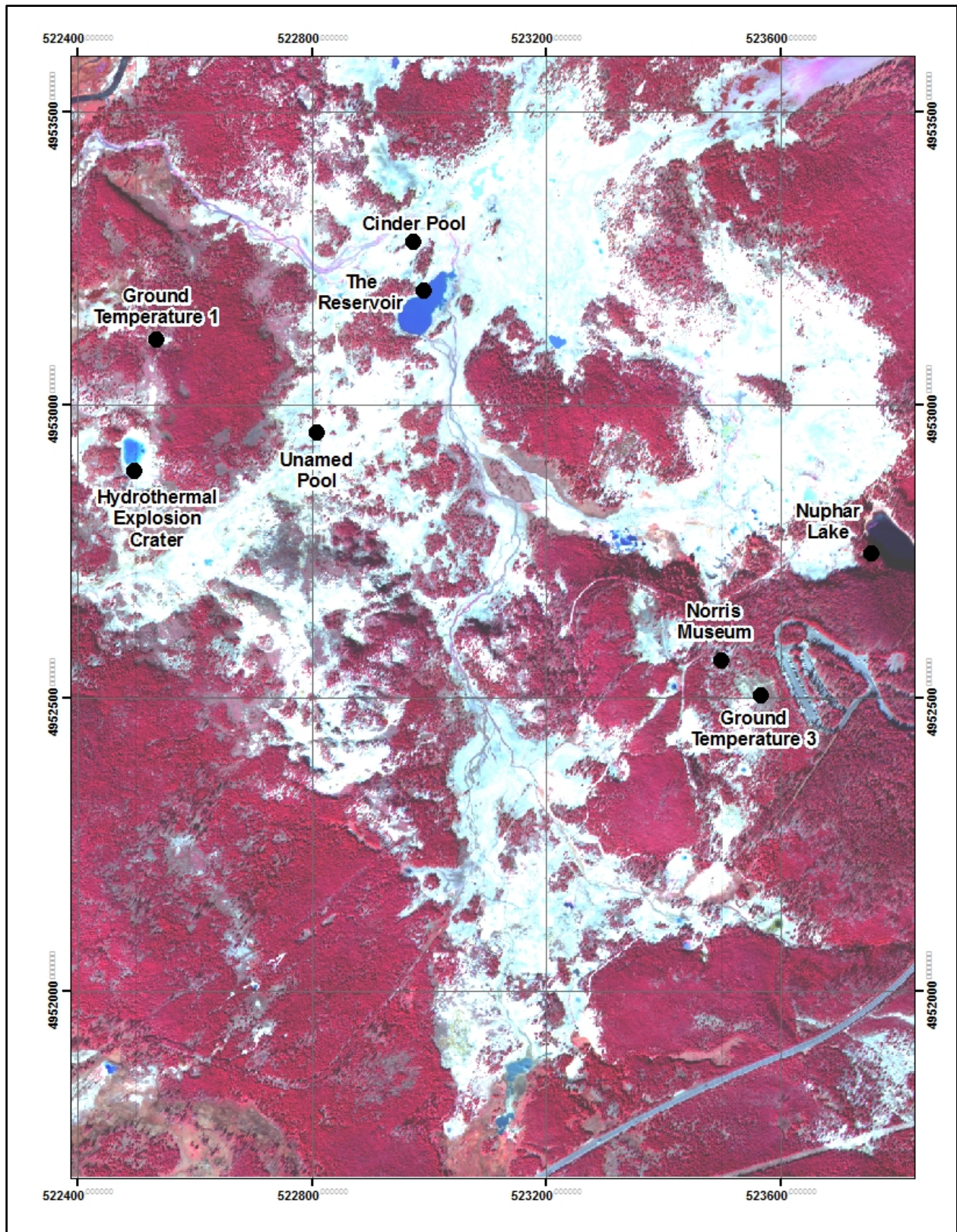


298 **Figure 3.** Graph showing air and surface ground temperatures within Norris Geyser Basin from
 299 September 7 through September 11, 2009. An infrared radiometer pointing to a hot, dry area
 300 labeled “Hydrothermal Explosion Crater” in Figure 4 measured the surface ground temperatures.
 301
 302

303 **3.2 Comparison of Kinetic and Radiative Temperatures**

304 The accessibility and dynamic hydrothermal system of Norris Geyser Basin allowed an
305 assessment of the derived radiative and measured kinetic temperature accuracy. Surface kinetic
306 temperatures measured at different ground locations provided the ground truth for an assessment
307 of the radiative temperatures derived from the corrected and calibrated airborne 2008 to 2011
308 TIR imagery. Five water bodies of varying size and kinetic temperatures (Figure 4) contained
309 temperature sensors during the times of the night-time TIR flights. In 2011, two additional sites
310 (Figure 4) had temperature sensors measuring ground temperatures during the nighttime TIR
311 flight.

312 Onset Computer Corporation temperature loggers measured kinetic surface temperatures
313 using two types of loggers: the Onset Hobo Pro and the Onset Microstation. Both loggers had 2-
314 m length thermistor probes, accurate to within 0.2 °C. Placement of loggers for water body
315 temperatures involved placing the thermistors approximately 1 to 5 cm below the water surface
316 and approximately 1.5 m from the shoreline. For ground temperatures, placement of thermistors
317 involved their burial 1 cm below the ground surface. Both the water body and ground
318 temperature loggers acquired temperature data at 1-minute intervals. Thermistors were placed at
319 hydrothermal pools with well-mixed temperatures and hydrothermally active ground (Table 2;
320 Figure 4). For each measurement site (Table 2), the approximate, measured ground kinetic
321 temperature, the area of the water bodies, and the associated comments provide additional
322 information on the sites chosen for this assessment.



323
 324 **Figure 4.** Orthorectified visible image (MSS-LiDAR) showing locations of kinetic temperature
 325 measurements in Norris Geyser Basin.

326
327
328
329
330
331
332
333

Hydrothermal pools of different temperatures enabled an assessment of the difference between calculated values of at-surface, radiative temperatures and measured kinetic ground temperatures. For three of the selected pools, bubbling gases (steam or carbon dioxide) mixed the hydrothermal waters at Cinder Pool, the Reservoir and the hydrothermal explosion crater and provided a pool with a near-constant temperature. Measuring the near-surface at the two ground temperatures in active, hydrothermally heated ground minimized the effect of solar heating on the surface of the ground.

334
335

Table 2. Characteristics of kinetic temperatures for locations.

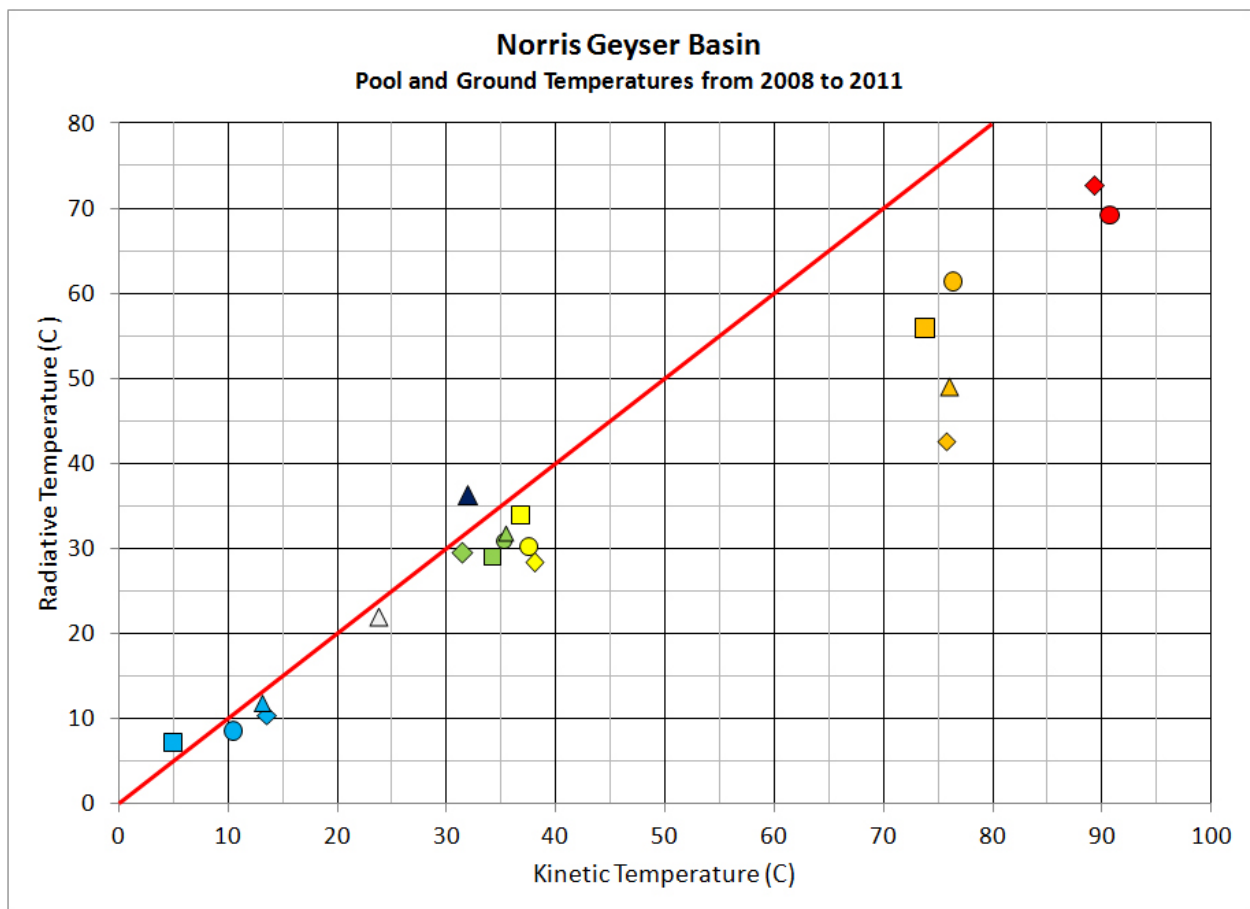
336

Name	Approximate Kinetic Temperature (Celsius)	Water Body Area (m ²)	Comments
Cinder Pool	90	162	Steam bubbles mix pool.
Unnamed Pool	76	92	Calm pool with minor outflow.
Hydrothermal Explosion Crater	30	1634	Carbon dioxide gas mixes pool.
The Reservoir	30	4815	Carbon dioxide gas mixes pool.
Nuphar lake	10	7715	Cool water lake with no surface hydrothermal input.
Ground Temperature 1	32	Not Applicable	
Ground Temperature 3	24	Not Applicable	

337
338
339
340
341
342

Comparison of calibrated and corrected TIR temperatures (2008 through 2011) with the measured kinetic temperatures yielded an assessment of the airborne technique's temperature accuracy. The GPS coordinates of the thermistors provided a location for selecting representative radiative temperatures from the night-time TIR image. The maximum calculated value of radiative temperature over 4 pixel (4 m²) area provided a reasonable estimate of

343 radiative temperature. An area of 4 pixels allowed for any positional inaccuracies during the
 344 production of the night-time TIR image mosaic. The 1-minute, ground temperature data
 345 recorded during airborne acquisitions afforded measured kinetic temperatures for comparison
 346 with calculated surface values of radiative temperatures. Results of the temperature comparison
 347 (Figure 5) showed that kinetic and radiative temperatures generally agreed for temperatures less
 348 than 35 °C. For kinetic temperatures greater than 35 °C, the root mean square error for the
 349 relationship is 19.1 °C with a mean bias error of -16.8 °C. For kinetic temperatures less than 35
 350 °C, the root mean square error is 3.3 °C with a mean bias error of -1.8 °C.



357 white diamond refers to Ground Temperature 3. Refer to Figure 4 for locations of temperature
358 measurement sites.

359
360 At higher temperatures, water vapor associated with the hydrothermal pools is the most
361 likely explanation for the lack of agreement between the measured kinetic and derived radiative
362 temperatures. The air temperature at Norris at the time of the flights ranged from -3.1 to 6.9 °C.
363 The relatively low air temperature and the high pool temperatures can cause a zone of high water
364 vapor above the pool and may lead to the formation of a water vapor cloud. Because water
365 vapor absorbs the 8 to 12 micron TIR energy, the calculated, radiative at-surface temperatures
366 generally is less than the measured kinetic, surface temperatures due to masking.

367 For their study in Alaska, Haselwimeimmer and others (2013) reported that airborne
368 radiometric temperatures at Pilgrim Hot Springs consistently underestimated ground kinetic
369 temperatures by ~2 to 3 °C. However, the maximum temperatures for their study were 58 °C,
370 well below the 75 °C to 91 °C measured in this study. Thus, Haselwimeimmer and others (2013)
371 encountered few problems associated with water vapor absorbing the thermal infrared energy at
372 high temperatures.

373 For the 2008 to 2011 night-time TIR mosaics, a qualitative assessment of spatial accuracy
374 involved Norris Geyser Basin's boardwalks and trails. Measuring the changing spatial location
375 of trail junctions within the 2008 to 2011 TIR mosaic provided a qualitative assessment of its
376 spatial accuracy yielded a spatial variability ranging from 2-6 m with higher accuracies obtained
377 after orthorectification using the LiDAR data was introduced in 2010. This assessment of the
378 spatial accuracy and temperature precision has implications for scientific visualizations of the
379 hydrothermal systems and geologic applications.

380

381 **4.0 APPLICATIONS TO THE HOT SPRING BASIN AND NORRIS GEYSER BASIN**

382 **HYDROTHERMAL SYSTEMS**

383 Two hydrothermal systems provide an application of the airborne TIR monitoring
384 technique described in the preceding paragraphs: Hot Spring Basin (HSB) and Norris Geyser
385 Basin (NGB) (Figure 1). The time-series for HSB cover the years 2007 to 2011 whereas the
386 time-series for NGB span the years 2008 to 2011. Although HSB is an acid-sulfate system and
387 NGB has acid sulfate and neutral chloride hydrothermal features, both hydrothermal systems
388 occur outside the 640,000 Yellowstone caldera. Fractured bedrock affects hydrothermal fluid
389 flow in both systems. Thus, a summary of the bedrock and surficial geology of both areas is
390 relevant.

391

392 **4.1 Relevant Geology**

393 Located north and east of the Sour Creek resurgent dome, heat, water and gases flow
394 through an extensive network of fractured volcanic rock and various Quaternary sediments thus
395 forming the Hot Spring Basin (HSB) hydrothermal system. Faulted and fractured 640,000 year
396 Lava Creek Tuff primarily comprises the bedrock (Christiansen and Blank, 1975; Prostka and
397 others, 1975a; Prostka and others, 1975b) within the HSB hydrothermal system (Figure 6).
398 Various glacial sediments from multiple glacial episodes cover the bedrock (Pierce, 1974a;
399 Pierce, 1974b; Richmond, 1977) (Figure 7). Jaworowski and others (2013) provided additional
400 details on the geologic setting of the HSB hydrothermal system, its fracture system, and field
401 observations.

402 Located outside the 640,000 year Yellowstone caldera, the NGB hydrothermal system
403 occurs at the southern end of the north-south-trending Mammoth-Norris corridor. The faulted

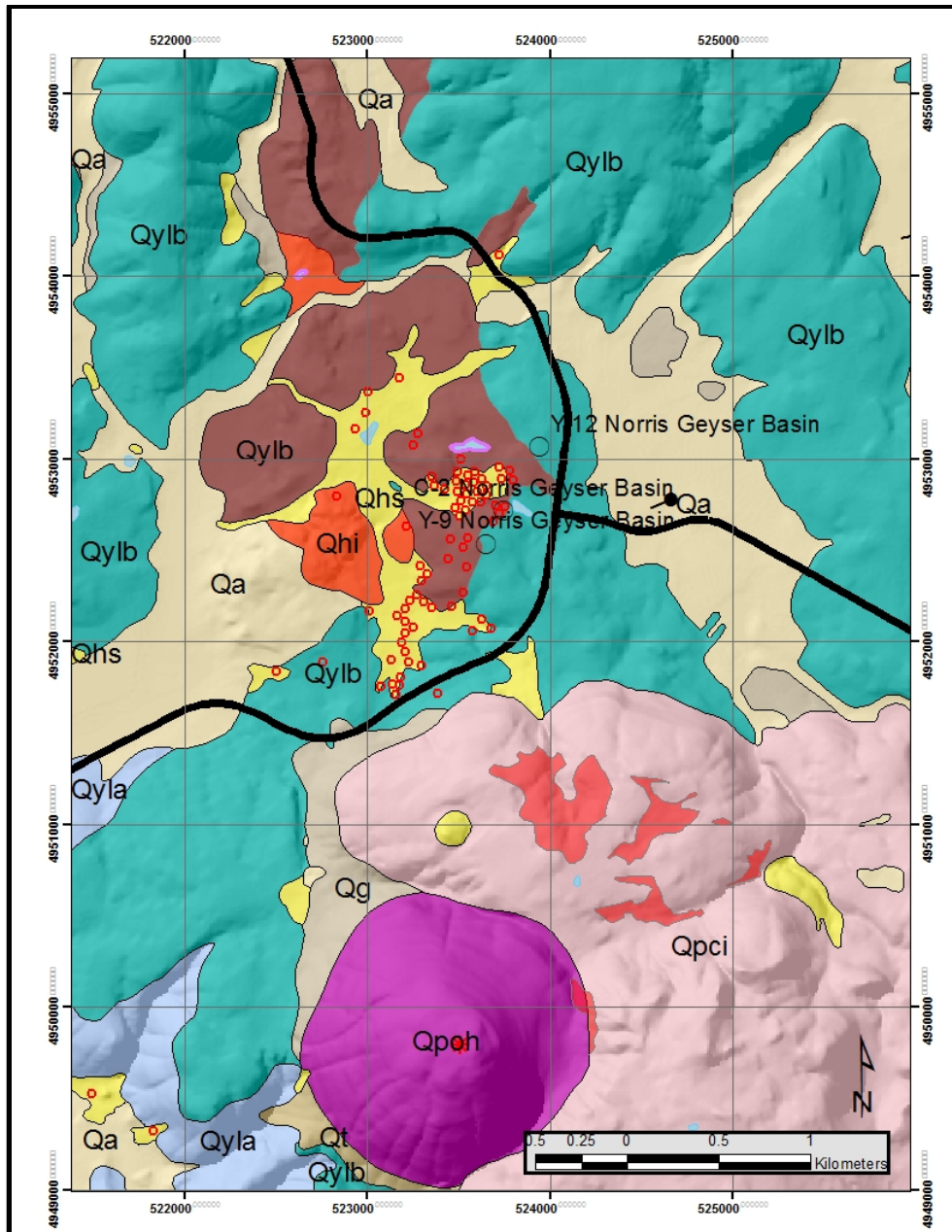
404 and fractured 640,000 year Lava Creek Tuff forms the bedrock for this hydrothermal system
405 (Christiansen, 1975; Figure 6). Hydrothermal deposits, alluvium, and various late glacial
406 sediments cover the hydrothermally altered rhyolitic tuff (Figure 7).

407 Numerous lava flows and domes formed along the recurrently faulted Mammoth-Norris
408 corridor (Christiansen, 2001). Post- Yellowstone caldera volcanic eruptions along this geologic
409 corridor began at 326,000 years with the most recent occurring at 56,000 years (Spell and others
410 2008). Scientists acknowledge that mafic input episodically recharges the magmatic system
411 along this geologically active corridor and introduces heat.

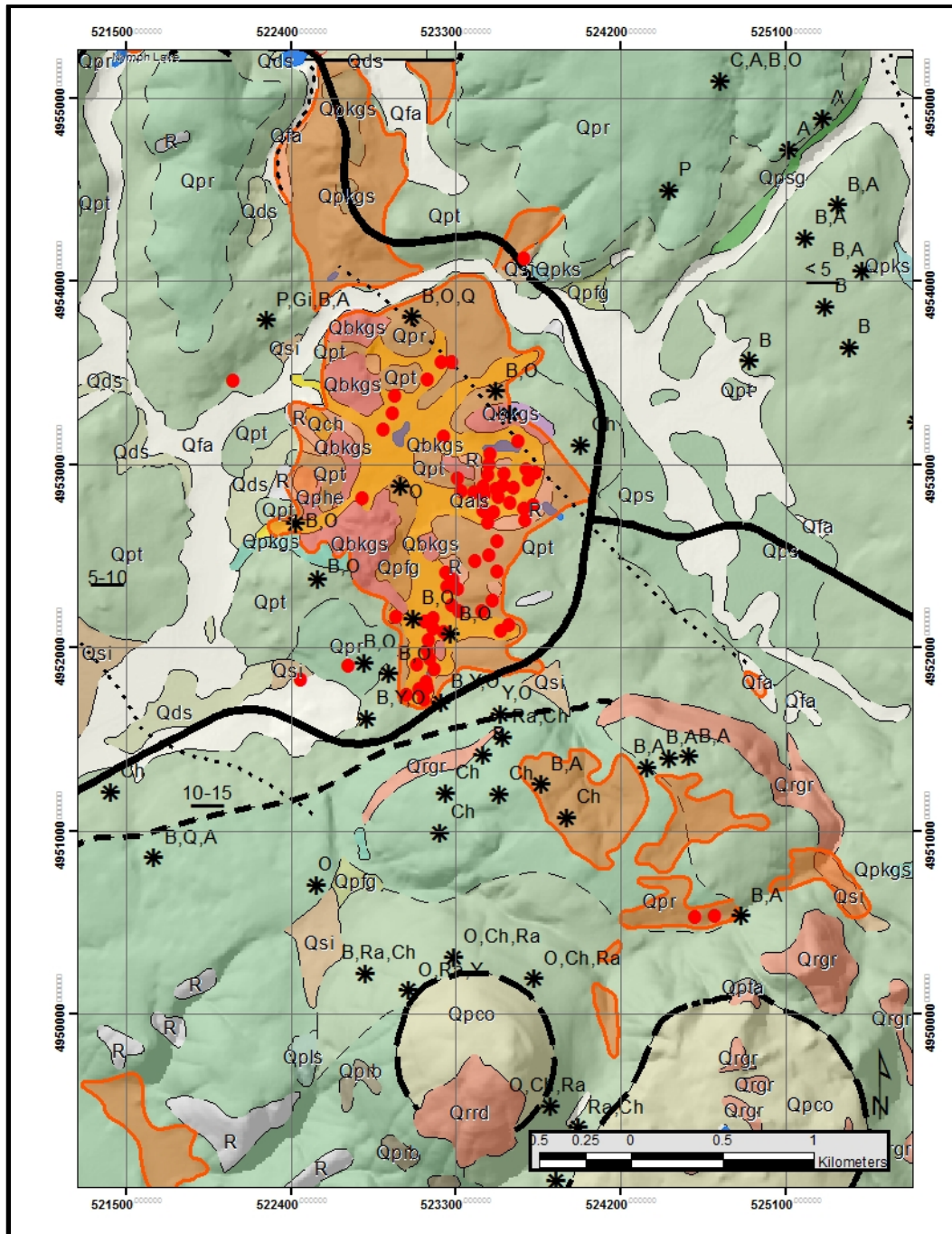
412 Norris Geyser Basin's highly fractured bedrock creates permeable pathways for fluid
413 flow. White and others (1988) recognized alignment of spring vents, tree lines, drainage patterns
414 and geologic features to the north, northwest and northeast. Jaworowski and others (2006)
415 recognized fracture permeability in the Lava Creek Tuff was responsible for the northeast and
416 northwest-trending zones of hydrothermal fluid flow on night-time TIR maps. Fournier and
417 others (1994) noted the temporal formation of acid-sulfate pools at Porcelain Terrace after the
418 1959 Hebgen Lake earthquake.

419 Patterns of documented ground deformation along the northern caldera rim are interesting
420 to consider when monitoring the Norris hydrothermal system. From 2004 to 2008, researchers
421 documented rapid uplift of the Sour Creek Dome and northern caldera rim subsidence (Dzurisin
422 and others, 2012; Chang and others, 2007). Chang and others (2007) documented a subsidence
423 rate of ~ 3 cm/year in the Norris area between 2004 and 2006. Rates of subsidence slowed from
424 2006 to 2007 with ~8 mm subsidence from September 2007 to September 2008 (Dzurisin and
425 others, 2012). Dzurisin and others (2012) state that "minor subsidence in the Norris area also
426 seems to have stopped by the third quarter of 2009, as indicated by the CGPS station NRWY".

427



428
 429 **Figure 6.** Map showing bedrock geology draped over a shaded digital elevation model for
 430 Norris Geyser Basin. Altered Lava Creek B (red-brown-Qylb) surrounds Norris Geyser Basin's
 431 siliceous hot spring deposits (Qhs) and extends northward along the main road (solid black line).
 432 Unaltered Lava Creek B (blue-green; Qylb), Lava Creek A (light blue; Qyla), and rhyolitic lava
 433 flows (Qpoh, Qpci) surround the altered tuff (Qylb). Till (tan; Qg), ice-contact deposits (orange;
 434 Qhi), and other sediments (light yellow; Qa) also crop out in the area. The map also shows the
 435 location of historic drill holes (C-2, Y-9 and Y-12) and hydrothermal features (red circles). The
 436 map's grid shows Universal Transverse Mercator (UTM) easting and northing coordinates.
 437 Road layer from Yellowstone Spatial Analysis Center. Original bedrock mapping by
 438 Christiansen (1975) and digital 15-minute geology compiled by National Park Service Geologic
 439 Resources Division (2007).
 440



441
 442 **Figure 7.** Map showing surficial geology draped over a shaded digital elevation model for
 443 Norris Geyser Basin. Various late glacial sediments (green; Qpt, Qps, Qpr, Qpfg, Qpsg), ice-
 444 contact deposits (Qpks), older glacial deposits (Qbkg), hydrothermal deposits (Qsi, ds, ch),
 445 alluvial deposits (Qfa), and bedrock (Qrrd, Qrgr, Qpco, R). Geologists also mapped various
 446 glacial erratics (black asterisks) and hydrothermal features (solid red circles). Original surficial
 447 mapping by Richmond and Waldrop (1975) and digital 15-minute geology compiled by National
 448 Park Service Geologic Resources Division (2007).
 449

450 **4.2 A New Perspective of Hydrothermal Systems**

451 A low temperature cut-off highlights the complex spatial patterns for each hydrothermal
452 system. For the Hot Spring Basin (HSB) time series of night-time TIR imagery (2007 to 2011),
453 a cut-off temperature of 10 °C eliminated the low-temperature components of the hydrothermal
454 system that could be significantly influenced by residual solar heating. For the Norris Geyser
455 Basin (NGB), time series of night-time TIR imagery (2008 to 2011), a low temperature cut-off of
456 5 to 9 °C eliminated the low-temperature components of the hydrothermal systems affected by
457 residual solar heating.

458 The time series of night-time TIR imagery (Figures 8 and 9a-d) for the HSB
459 hydrothermal system documented the natural variability of temperature and fluid-flow within
460 this fracture-dominated system. Hydrothermal waters flow through fractured Lava Creek Tuff
461 and overlying sediments into Shallow Creek and Wrong Creek. Major north-south trending
462 basins, alignments of hydrothermal features in the night-time TIR imagery and the LiDAR
463 lineaments show the hydrothermal system's fracture permeability. For the September 2007 to
464 2011 time series, the National Science Foundation (NSF) Earthscope LIDAR forms the base map
465 (refer to www.opentopography.org) for all temperature components of the central HSB
466 hydrothermal system. The time-temperature series shows high-temperature components (red
467 color; >40°C) and intermediate-temperature components (orange, yellow, green and light blue; >
468 10°C and < 40°C) for the Main and East basins. From 2007 to 2011, the least variability within
469 the central HSB hydrothermal system occurred in the Main Basin with its numerous fumaroles.
470 From 2007 to 2011, the greatest variability occurred in the East Basin with its numerous
471 hydrothermal pools. Between the 2007 and 2008 image acquisitions, new hydrothermal activity
472 developed along a north-south trending fracture at the north-end of the Main Basin (Jaworowski

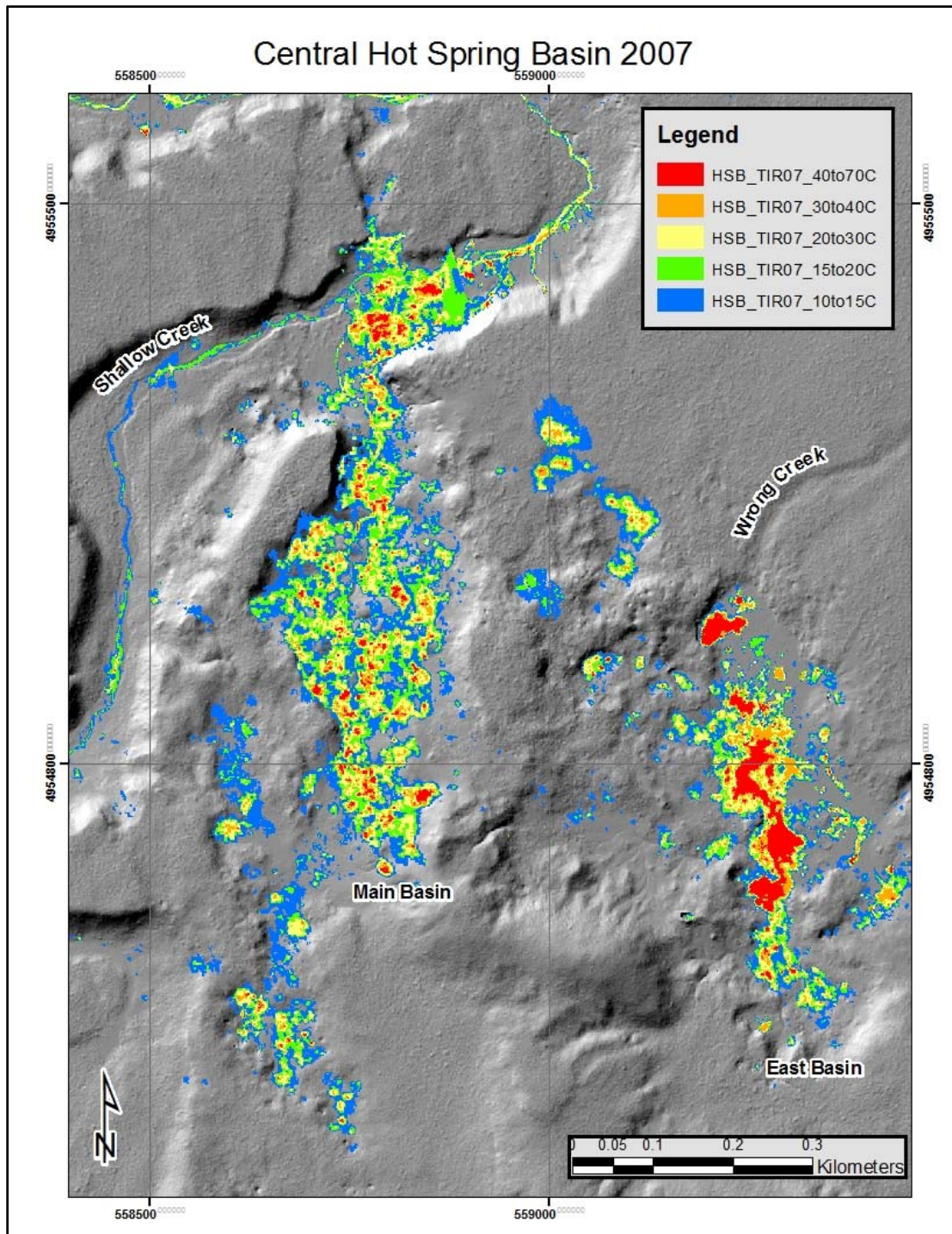
473 and others, 2013). Comparison of figures 8 and 9a shows contiguous hydrothermal activity north
474 of Shallow Creek in the 2008 night-time TIR image. A change in hydrothermal alteration of the
475 ground surface between 2006 and 2008 confirmed that this slight change in the spatial
476 temperature pattern along the northern portion of the Main Basin was the result of changing
477 hydrothermal activity within the central HSB hydrothermal system.

478 Natural fractures within the Lava Creek Tuff also control hydrothermal fluid flow within
479 the NGB hydrothermal system (Figures 10a-d) and the night-time TIR imagery reflects the
480 hydrothermal fluid flow along these northwest-and northeast-trending fractures. Norris Geysers
481 Basin is an unusual hydrothermal system in Yellowstone because a single northwest-flowing
482 creek, Tantalus Creek (yellow and green colors; 30°C to 15°C), captures 98% of the thermal
483 discharge of NGB (Friedman, 2007) and flows into the sinuous Gibbon River. The high-
484 temperature components (red color; >40°C) and intermediate-temperature components (orange,
485 yellow, green and light blue; > 10°C and < 40°C) components of the hydrothermal system show
486 the preferred orientation of hydrothermal fluids along northeast- and northwest-trending
487 fractures. High temperature components (red color; >40°C), intermediate temperature
488 components (orange, yellow, green and light blue; > 10°C and < 40°C) and low temperature
489 components (dark blue; <10°C) are different between the 2008, 2009, and 2010 TIR imagery
490 components. Significant differences exist between the 2008 and 2011 temperature components
491 for Porcelain Basin that show increased hydrothermal activity. This increase in hydrothermal
492 activity for Porcelain Basin correlates with field observations. Additionally, the Back Basin
493 shows interesting differences in the vicinity of Pearl Geysers from 2008 to 2011 while other areas
494 such as the Reservoir appear remarkably consistent from 2008 to 2011. Low temperature

495 components (dark blue; <10°C) provide a visualization of the spatial extent of the NGB
496 hydrothermal system.

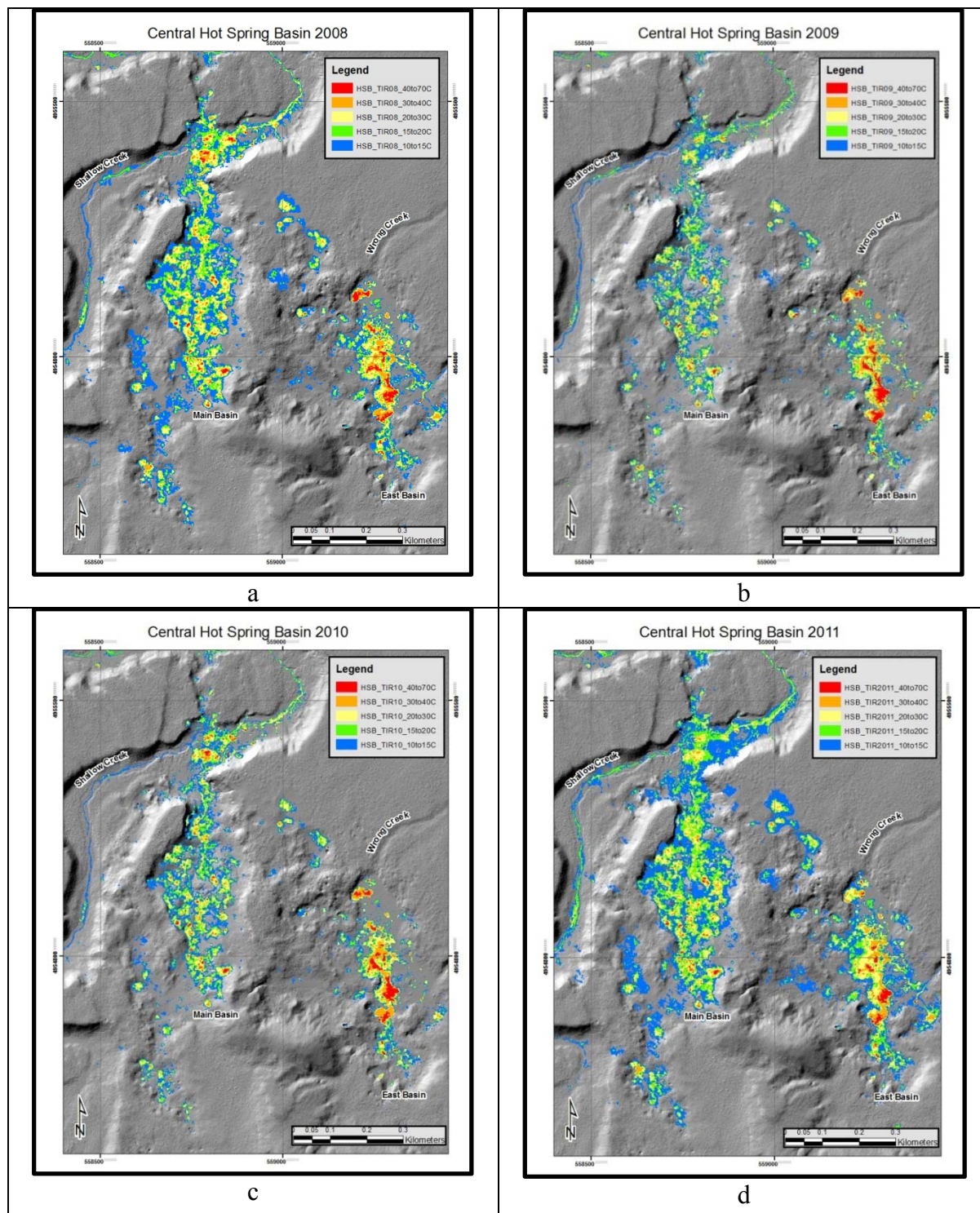
497 The 1-m spatial resolution of the night-time TIR airborne imagery documented a variable
498 and complex pattern of surface temperatures and hydrothermal fluid flow. For display of these
499 complex spatial patterns, the temperature components (high, intermediate and low) of the
500 hydrothermal systems provide reasonable scientific visualizations given the assessment of
501 temperature and spatial accuracy. Environmental differences between the acquisitions may be
502 responsible for some variability in scientific visualizations of the HSB and NGB hydrothermal
503 systems. For example, the earliest flight time and warmest air temperature occurred during the
504 September 2011 image acquisition. However, it is important to emphasize that the time series of
505 images do show similar hydrothermal patterns from year to year and also allow the visualization
506 of changes within the hydrothermal system.

507

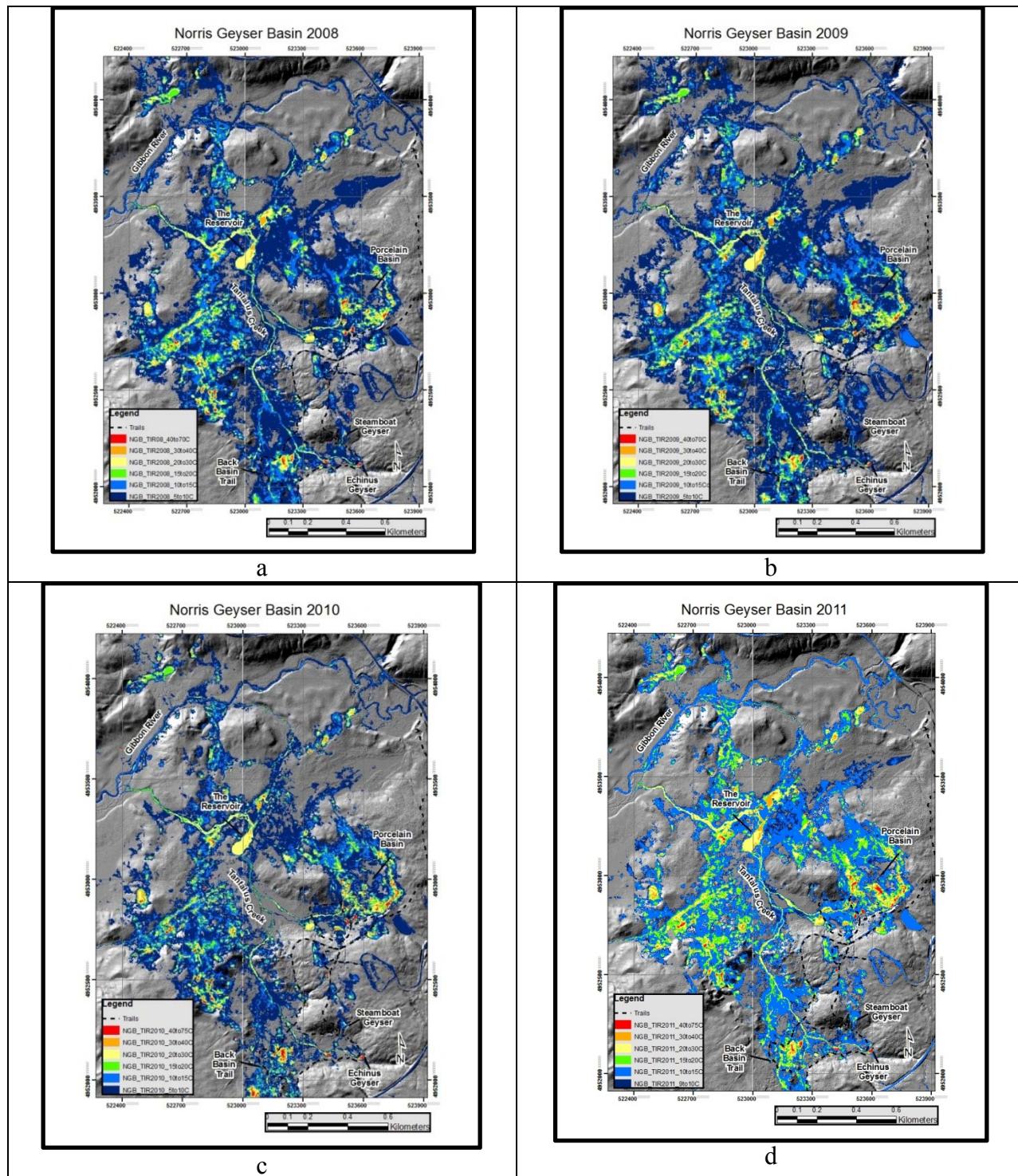


508

509 **Figure 8.** Night-time, TIR radiometric temperature map of the central Hot Spring Basin (HSB)
 510 hydrothermal system for September 2007. Map shows high temperature components (red color;
 511 $>40^{\circ}\text{C}$) and intermediate temperature components (orange, yellow, green and light blue; $> 10^{\circ}\text{C}$
 512 and $< 40^{\circ}\text{C}$) for the Main and East basins. Shallow Creek flows through the western portion of
 513 the central HSB hydrothermal system and Wrong Creek has its headwaters in the central and
 514 eastern portions of the HSB hydrothermal system. The NSF Earthscope LIDAR provides the
 515 base map (shaded grey) for the temperature components of the HSB hydrothermal system.



517 **Figure 9 a-d.** Night-time TIR radiometric temperature maps showing high (red) and
 518 intermediate (orange, yellow, green, and light blue) temperature components of the central Hot
 519 Spring Basin hydrothermal system with its north-south trending hydrothermal basins for
 520 September 2008 (a), 2009 (b), 2010 (c) and 2011 (d). NSF Earthscope LIDAR base map (shaded
 521 grey).



522 **Figure 10 a-d.** Night-time, TIR radiometric temperature maps showing high (red) and
 523 intermediate (orange, yellow, green, and light blue) temperature components of Norris Geyser
 524 Basin (NGB) hydrothermal system for September 2008 (a), 2009 (b), 2010 (c) and 2011 (d).
 525 NSF Earthscope LIDAR base map (shaded grey).

526 **5.0 FUTURE WORK**

527 Future research will concentrate on field experiments and gathering data to study the
528 effects of solar heating and radiative cooling as a function of air temperature, wind speed and
529 humidity and how this varies at different times of the year. This future work will allow for the
530 development of methods that may compensate for residual solar heating in the imagery and the
531 presence of steam over hot pools, ultimately improving the precision of calculated, radiative
532 surface temperatures from the airborne imagery.

533

534 **6.0 CONCLUSIONS**

535 Airborne thermal infrared remote sensing has the spatial resolution necessary for
536 documenting basin-wide changes within hydrothermal systems and the formation of new
537 hydrothermal activity in Yellowstone National Park. It also allows flexibility to plan the image
538 acquisitions for minimal residual solar heating effects. The technique did yield night-time
539 thermal infrared imagery of Norris Geyser Basin and Hot Spring Basin with 1-m spatial
540 resolution. Although the ambitious goal of 1°C accuracy was not met, the time series of
541 reproducible results documented and detected change within the Hot Spring Basin and Norris
542 Geyser Basin hydrothermal systems. Visualizations of the Hot Spring Basin and Norris Geyser
543 Basin hydrothermal systems captured the variability of temperature and hydrothermal fluid flow
544 and showed the value of high-spatial resolution, nighttime TIR, airborne imagery for monitoring
545 these systems.

546

547

548 **7.0 ACKNOWLEDGEMENTS**

549 This research would not have been possible without the support of numerous individuals
550 and institutions. The National Park Service Rocky Mountain Cooperative Ecological Study
551 Units Agreements (RM-CESU J1580050583, J1580050608, and J1580090425) provided funds
552 for thermal infrared research of Hot Spring Basin, Norris Geyser Basin and other hydrothermal
553 systems. The Remote Sensing Services Laboratory in the Dept. of Civil and Environmental
554 Engineering at Utah State University and the Utah Agricultural Experiment Station also provided
555 support. The LASSI Lidar and imaging system was developed with funds from the Utah
556 Science Technology and Research initiative (USTAR) at Utah State University.

557

558 8.0 REFERENCES CITED

559

560 Allen, R. G, Tasumi, M., and Trezza, R. (2007). Satellite-Based Energy Balance for Mapping
561 Evapotranspiration with Internalized Calibration MET—Model. *Journal of Irrigation and*
562 *Drainage Engineering*, 133(4).

563

564 Berk, A., Bernstein, L.S., and Robertson, D.C. (1989): MODTRAN: a moderate resolution
565 model for LOWTRAN 7. *Report GL-TR-89-0122. Geophysics Laboratory, Bedford, Maryland,*
566 *USA.*

567

568 Brunsell, N.A., & Gillies, R. (2002). Incorporating Surface Emissivity into a Thermal
569 Atmospheric Correction. *Photogrammetric Engineering & Remote Sensing Journal (ASPRS)*,
570 68(12), 1263-1269.

571

572 Cai, B. & Neale, C. M. U. (1999). A Method for Constructing 3-Dimensional Models from
573 Airborne Imagery. In: *Color Photography and Videography for Resource Assessment.*
574 *Proceedings of the 17th Biennial Workshop. American Society for Photogrammetry and Remote*
575 *Sensing, Bethesda, MD.*

576

577 Cardenas, B.M., Neale, M.U., Jaworowski, C., & Heasler, H. (2011). High-resolution mapping
578 of river-hydrothermal water mixing. *International Journal of Remote Sensing*, 32(10), 2765-
579 2777.

580

581 Chang, W-L, Smith, R.B., Wicks, C., Farrell, J.M., & Puskas, C.M. (2007). Accelerated uplift
582 and magmatic intrusion of the Yellowstone caldera, 2004 to 2006. *Science*, 318(5852), 952-956.

583
584 Chávez, J. L., Neale, C. M. U., Hipps, L. E., Prueger, J. H., & Kustas. W. P. (2005). Comparing
585 aircraft-based remotely sensed energy balance fluxes with eddy covariance tower data using heat
586 flux source area functions. *Journal of Hydrometeorology*, 6(6), 923–940.

587
588 Christiansen, R, L. (2001) The Quaternary and Pliocene Yellowstone Plateau Volcanic Field of
589 Wyoming, Idaho, and Montana. *U.S. Geological Survey Professional Paper 729-G*, 145 pp.

590
591 Christiansen, R .L. (1975). Geologic Map of the Norris Junction Quadrangle, Yellowstone
592 National Park, Wyoming. *U.S. Geological Survey Geologic Quadrangle Map GQ-1193, Scale*
593 *1:62,500*.

594
595 Christiansen, R. L., & Blank. H. Jr. (1975). Geologic Map of the Canyon Village Quadrangle,
596 Yellowstone National Park *U.S. Geologic Survey Geologic Quadrangle Map GQ-1192, Scale*
597 *1:62,500*.

598
599 Christiansen, R. L. (1966). Preliminary evaluation of radar imagery of the Yellowstone rhyolite
600 plateau. In Preliminary evaluation of radar imagery of Yellowstone National Park, Wyoming.
601 *Technical Letter NASA-30 prepared by the U.S. Geological Survey for the National Aeronautics*
602 *and Space Administration, under NASA Contract No. R-09-020-015, Task No. 160-75-01-44-10*.

603

604 Dzurisin, D., Wicks, C. W., & Poland, M.P. (2012). History of Surface Displacements at the
605 Yellowstone Caldera, Wyoming, from leveling surveys and InSAR Observations, 1923-2008:
606 *U.S. Geological Survey Professional Paper 1788*, 68 pp.

607

608 Friedman, I. (2007). Monitoring changes in geothermal activity at Norris Geyser Basin by
609 satellite telemetry, Yellowstone National Park, Wyoming *in* :L.A, Morgan (ed), Integrated
610 Geoscience Studies in the Greater Yellowstone Area. *U.S. Geological Survey Professional Paper*
611 *1717*, 513-532.

612

613 Geli, Hatim M. E.; Neale, Christopher M. U.; Watts, Doyle; Osterberg, J; De Bruin, HAR;
614 Kohsiek, W; Pack, RT; Hipps, LE. (2012). Scintillometer-Based Estimates of Sensible Heat
615 Flux Using Lidar-Derived Surface Roughness. *JOURNAL OF HYDROMETEOROLOGY*,
616 Volume: 13 Issue: 4 Pages: 1317-1331

617

618 Hardy, C.C. (2005). *Characterizing thermal features from multi-spectral remote sensing data*
619 *using dynamic calibration procedures*. Missoula, Montana: University of Montana (Ph.D), 153
620 pp.

621

622 Haselwimmer, C., Prakash, A, & Holdmann, G. (2013). Quantifying the heat flux and outflow
623 rate of hot springs using airborne thermal imagery: Case study from Pilgrim Hot Springs, Alaska.
624 *Remote Sensing of Environment*, 136, 37-46.

625

626 Jaworowski, C., Heasler, H .P., Neale, C. M. U., Sivarajan, S., & Ashish, M. (2013). Temporal
627 and Spatial Variations of the Hot Spring Basin Hydrothermal System, Yellowstone National
628 Park, USA. *Remote Sensing*, 5(12), 6587-6610.

629

630 Jaworowski, C., Heasler, H .P., Neale, C. M .U., & Sivarajan, S. (2012) Monitoring the Dynamic
631 Geohydrology of the Upper Geyser Basin, Yellowstone National Park- An Integration of
632 Airborne Thermal Infrared and LIDAR Imagery. *Proceedings of 2010 Remote Sensing and
633 Hydrology Symposium September 2010, IAHS-AISH publication (2012)*, 54-58.

634

635 Jaworowski, C., Heasler, H. P., Hardy, C. C., & Queen, L .P, (2006). Control of Hydrothermal
636 Fluids by Natural Fractures at Norris Geyser Basin. *Yellowstone Science*, 14(4), 13-23.

637

638 Kustas W. P. & Norman, J.M. (1999). Evaluation of soil and vegetation heat flux predictions
639 using a simple two-source model with radiometric temperatures for partial canopy cover. *Agric.
640 For. Meteor*, 94, 13-29.

641

642 Li, F., Kustas, W. P., Prueger, J. H., Neale, C. M. U., & Jackson, J. T. 2005. Utility of Remote
643 Sensing Based Two-Source Energy Balance Model Under Low and High Vegetation Cover
644 Conditions. *J Hydrometeorology*, 6, 878-891.

645

646 Li, Z. L., Tang, B. H., Wu, H., Ren, H. Z., Yan, G.J., Wan, Z. M., Trigo, I.F., & Sobrino, J.A.
647 (2013). Satellite-derived land surface temperature: Current status and perspectives. *Remote
648 Sensing of Environment*, 131, 14-37.

649

650 Livo, K. E., Clark, R. N., Kruse, F. A., & Kokaly, R. F. (1999). Characterization of
651 hydrothermally altered rock and hot spring deposits at Yellowstone National Park using AVIRIS
652 data. *Jet Propulsion Laboratory Report: JPL-99-17. Boulder, Co., USGS Spectroscopy*
653 *Laboratory, 259-266, 8 pp.*

654

655 Mia, M. B., Bromley, C., & Fujimitsu, Y. (2013). Monitoring Heat Losses Using Landsat ETM
656 plus Thermal Infrared Data: a Case Study in Unzen Geothermal Field, Kyushu, Japan. *Pure and*
657 *Applied Geophysics, 170(12), 2263-2271*

658

659 Neale, C. M.U., H. M.E. Geli, W. P. Kustas, J. G. Alfieri, P. H. Gowda, S. R. Evett, J.H.
660 Prueger, L. E. Hipps, W. P. Dulaney, J. L. Chávez, A. N. French, T. A. Howell. (2012). Soil
661 water content estimation using a remote sensing based hybrid evapotranspiration modeling
662 approach. *Advances in Water Resources, Volume 50, December 2012, Pages 152-161, ISSN*
663 *0309-1708, 10.1016/j.advwatres.2012.10.008.*

664

665 Neale, M.U., & Sivarajan, S. (2011). Airborne Thermal Infrared Mapping of Hydrothermal
666 Springs and Features in Geyser Basins of Yellowstone National Park. *Final report for Task*
667 *Agreement Numbers J1580090425 and J1580050608, 22 pp.*

668 [http://www.cfc.umt.edu/CESU/Reports/NPS/USU/2005/05_08Neale_YELL_%20Thermal_Final](http://www.cfc.umt.edu/CESU/Reports/NPS/USU/2005/05_08Neale_YELL_%20Thermal_Final_Report.pdf)
669 [_Report.pdf](http://www.cfc.umt.edu/CESU/Reports/NPS/USU/2005/05_08Neale_YELL_%20Thermal_Final_Report.pdf)

670

671 Neale, C. M. U., Geli, H., Taghvaeian, S., Masih, A., Pack, R. T., Simms, R.D., Baker, M.,
672 Milliken, J.A., O'Meara, S., & Witherall, A.J. (2011). Estimating evapotranspiration of riparian
673 vegetation using high resolution multispectral, thermal infrared and lidar data. In *SPIE Remote*
674 *Sensing, International Society for Optics and Photonics*, 81740P-81740P.

675

676 Neale, C. M. U., & Crowther. B. (1994). An airborne multispectral video/radiometer remote
677 sensing system: development and calibration. *Remote Sensing of Environment*, 49(3), 187-194.

678

679 Norman J. M., Kustas, W. P. & Humes, K.S. (1995). A two-source approach for estimating soil
680 and vegetation energy fluxes in observations of directional radiometric surface temperature.
681 *Agric. For. Meteor.* 77, 263-293.

682

683 National Park Service Geologic Resources Division, 2007, Digital compilation of original
684 U.S.G.S. 15-minute bedrock maps for Yellowstone National Park by NPS Geologic Resources
685 Division, retrieved from <https://irma.nps.gov/App/Portal/Home>

686

687 National Park Service Geologic Resources Division, 2007, Digital compilation of original
688 U.S.G.S. 15-minute surficial geologic maps for Yellowstone National Park by NPS Geologic
689 Resources Division, retrieved from <https://irma.nps.gov/App/Portal/Home>

690

691 Pierce, K .L, (1968). Evaluation of infrared imagery applications to studies of surficial geology
692 in Yellowstone Park. *Technical Letter NASA-93 prepared by the U.S. Geological Survey for the*

693 *National Aeronautics and Space Administration under NASA Contract No. R-09-020-015, Task*
694 *No. 160-75-01-44-10.*

695

696 Pierce, K. L. (1974a). Surficial Geologic Map of the Tower Junction Quadrangle and Part of the
697 Mount Wallace Quadrangle, Yellowstone National Park, Wyoming and Montana. *U.S. Geologic*
698 *Survey Miscellaneous Field Investigation Map I-647, Scale 1:62,500.*

699

700 Pierce, K. L. (1974b). Surficial Geologic Map of the Abiathar Peak and parts of the adjacent
701 Quadrangles, Yellowstone National Park, Wyoming and Montana. *U.S. Geologic Survey*
702 *Miscellaneous Field Investigation Map I-646, Scale 1:62,500.*

703

704 Prostka, H. J. (1966). Preliminary general evaluation of radar imagery in Yellowstone Park. *in*
705 *Preliminary general evaluation of radar imagery in Yellowstone Park. Technical Letter NASA-30*
706 *prepared by the U.S. Geological Survey for the National Aeronautics and Space Administration,*
707 *under NASA Contract No. R-09-020-015, Task No. 160-75-01-44-10.*

708

709 Prostka, H. J., Blank, H. R. Jr., Christiansen, R. L., & Ruppel, E. T. (1975a). Geologic Map of
710 the Tower Junction Quadrangle, Yellowstone National Park, Wyoming and Montana. *U.S.*
711 *Geologic Survey Geologic Quadrangle Map GQ-1247, Scale 1:62,500.*

712

713 Prostka, H. J., Blank, H. R. Jr., Christiansen, R. L., & Ruppel, E. T. (1975b). Geologic Map of
714 the Tower Junction Quadrangle, Yellowstone National Park, Wyoming and Montana. *U.S.*
715 *Geologic Survey Geologic Quadrangle Map GQ-1247, Scale 1:62,500.*

716

717 Richmond, G. M, and Waldrop, H. A. (1975). Surficial Geologic Map of the Norris Junction
718 Quadrangle, Yellowstone National Park. *U.S. Geological Survey Miscellaneous Geologic*
719 *Investigations Map I-650, Scale 1:62,500.*

720

721 Richmond, G.L.(1977). Surficial Geologic Map of the Canyon Village Quadrangle, Yellowstone
722 National Park, Wyoming. *U.S. Geologic Survey Miscellaneous Field Investigation Map I-652,*
723 *Scale 1:62,500.*

724

725 Roberts, D. A., Quattrochi, D. A., Hulley, G. C., Hook, S. J.; & Green, R. O. (2012). Synergies
726 between VSWIR and TIR data for the urban environment: An evaluation of the potential for the
727 Hyperspectral Infrared Imager (HyspIRI) Decadal Survey mission. *Remote Sensing of*
728 *Environment, 117, 83-101.*

729

730 Ruppel, E.T. (1966). Preliminary general evaluation of radar imagery in Yellowstone Park in
731 southern Gallatin Range and vicinity (Flights 89-#1, 89-#2, 89-#3, 94-2). *in Preliminary general*
732 *evaluation of radar imagery in Yellowstone Park. Technical Letter NASA-30 prepared by the*
733 *U.S. Geological Survey for the National Aeronautics and Space Administration under NASA*
734 *Contract No. R-09-020-015, Task No. 160-75-01-44-10.*

735

736 Savage, S.L., Lawrence, R.L., Custer, S.G., Jewett, J.T., Powell, S.L., & Shaw, J.A. (2010).
737 Review of Alternate Methods for Estimating Terrestrial Emittance and Geothermal Heat Flux for

738 Yellowstone National Park Using Landsat Imagery: *GIScience & Remote Sensing*, 47(4), 460-
739 479.

740

741 Seielstad, C. & Queen, L. (2009). Thermal Remote Monitoring of Norris Geyser Basin and
742 Associated Geothermal Resources, Yellowstone National Park, *Final Report for Task Agreement*
743 *Number J1580050583*, 33 pp.
744 http://www.cfc.umt.edu/CESU/Reports/NPS/UMT/2005/05_06Seielstad_YELL_thermal_final%20rpt.pdf
745

746 Smedes, H.W. (1968). Geological evaluation of infrared imagery, eastern part of Yellowstone
747 National Park, Wyoming and Montana. *Technical Letter NASA-83 prepared by the U.S.*
748 *Geological Survey for the National Aeronautics and Space Administration, Denver under NASA*
749 *Contract No. R-09-020-015, Task No. 160-75-01-44-10.*

750

751 Spell, T.L., Wooton, K., Nastanski, N., & Smith, E.I., (2008). The role of basalt in eruptions of
752 Quaternary rhyolites north of the Yellowstone caldera: *Geological Society of America 104th*
753 *Annual Meeting Cordilleran Section.*

754

755 Sundararaman, S. & Neale, C. M. U. (1997). Geometric Calibration of the USU Videography
756 System. Videography and Color Photography for Resource Assessment. *Proceedings of the 16th*
757 *Biennial Workshop. American Society for Photogrammetry and Remote Sensing, Bethesda, MD.*
758

759 Torgesen, C.E., R.N. Faux, R. N., Mcintosh, B. A., Poage, N. J., & Norton, D. J. (2001).
760 Airborne thermal remote sensing for water temperature assessment in rivers and streams. *Remote*
761 *Sensing of Environment* 76, 386-398

762

763 Quattrochi, D.A & J.C. Luvall. (2003) Thermal Remote Sensing in Land Surface Processes.

764 CRC Press, Boca Raton, Florida

765

766 Watson, F. G. R., Lockwood, R. E., Newman, W. B., Anderson, T. N., & Garrott, R. A. (2008).

767 Development and Comparison of Landsat Radiometric and Snow-pack Model Inversion

768 Techniques for Estimating Geothermal Heat Flux, *Remote Sensing of the Environment*, 112(2),

769 471-481.

770

771 White, D. E. Hutchinson, R. A., and Keith, T. E. C. (1988). The geology and remarkable thermal

772 activity of Norris Geyser Basin, Yellowstone National Park, Wyoming. *U.S. Geological Survey.*

773 *Professional Paper 1456*, 84 p.

774

775 Vaughan, R.G., Kezthelyi, L.P., Lowenstern, J.B., Jaworowski, C., and Heasler, H., (2012). Use

776 of ASTER and MODIS thermal infrared data to quantify heat flow and hydrothermal change at

777 Yellowstone National Park. *Journal of Volcanology and Geothermal Research*, 233-234, 72-89.

778